To cite this version :

Jamie FRAME, Laurent CORTÉ, Rachele ALLENA, Pierre-Yves ROHAN - A mechano-biological model of multi-tissue evolution in bone - Continuum Mechanics and Thermodynamics - Vol. 31, p.1-31 - 2019

Jamie Frameⓘ · **Pierre-Yves Rohan** · **Laurent Corté** ·
Rachele Allena

A mechano-biological model of multi-tissue evolution in bone

Abstract Successfully simulating tissue evolution in bone is of significant importance in predicting various biological processes such as bone remodeling, fracture healing and osseointegration of implants. Each of these processes involves in different ways the permanent or transient formation of different tissue types, namely bone, cartilage and fibrous tissues. The tissue evolution in specific circumstances such as bone remodeling and fracturing healing is currently able to be modeled. Nevertheless, it remains challenging to predict which tissue types and organization can develop without any a priori assumptions. In particular, the role of mechano-biological coupling in this selective tissue evolution has not been clearly elucidated. In this work, a multi-tissue model has been created which simultaneously describes the evolution of bone, cartilage and fibrous tissues. The coupling of the biological and mechanical factors involved in tissue formation has been modeled by defining two different tissue states: an immature state corresponding to the early stages of tissue growth and representing cell clusters in a weakly neo-formed Extra Cellular Matrix (ECM), and a mature state corresponding to well-formed connective tissues. This has allowed for the cellular processes of migration, proliferation and apoptosis to be described simultaneously with the changing ECM properties through strain driven diffusion, growth, maturation and resorption terms. A series of finite element simulations were carried out on idealized cantilever bending geometries. Starting from a tissue composition replicating a mid-diaphysis section of a long bone, a steady-state tissue formation was reached over a statically loaded period of 10,000 h (60 weeks). The results demonstrated that bone formation occurred in regions which are optimally physiologically strained. In two additional 1000 h bending simulations both cartilaginous and fibrous tissues were shown to form under specific geometrical and loading cases and cartilage was shown to lead to the formation of bone in a beam replicating a fracture healing initial tissue distribution. This finding is encouraging in that it is corroborated by similar experimental observations of cartilage leading bone formation during the fracture healing process. The results of this work demonstrate that a multi-tissue mechano-biological model of tissue evolution has the potential for predictive analysis in the design and implementations of implants, describing fracture healing and bone remodeling processes.

J. Frame (✉) · P. Rohan · R. Allena
LBM – Institut de Biomécanique Humaine Georges Charpak, ENSAM Paris, Paris, France
E-mail: jamie.frame@ensam.eu

L. Corté
Centre des Matériaux – CNRS : UMR7633, MINES ParisTech, PSL Research University, Paris, France

L. Corté
Matière Molle et Chimie – CNRS : UMR 7167, ESPCI Paris, PSL Research University, Paris, France

List of symbols

φ_{TOT}	Total volume fraction
$\varphi_{i,\text{TOT}}$	Total volume fraction of bone, cartilage and fibrous tissues, where $i = B, C\,or\,F$
φ_V	Total volume fraction of free space
φ_i^I	Volume fraction of immature bone, cartilage and fibrous tissues, where $i = B, C\,or\,F$
φ_i^M	Volume fraction of mature bone, cartilage and fibrous tissues, where $i = B, C\,or\,F$
ε_I	First principal strain
ε_{II}	Second principal strain
ε_Y	Yield strain
$\varepsilon_{k,N}$	Normalized principal strain where $k = I\,or\,II$.
$f_{i,k}\left(\varepsilon_{k,N}\right)$	Function relating the normalized principal strain with the rate of change of the activation time $t_{\text{act},i}$, where $i = B, C\,or\,F$ and $k = I\,or\,II$.
$a_{i,k}^\varepsilon, b_{i,k}^\varepsilon$	and $kc_{i,k}^\varepsilon$ Characteristic coefficients which define $f_{i,k}\left(\varepsilon_{k,N}\right)$ where $i = B, C\,or\,F$ and $k = I\,or\,II$.
$t_{\text{act},i}$	Activation time for each tissue, where $i = B, C\,or\,F$
$t_{\text{act}}^{\text{Bound}}$	Gaussian distribution used to limit the growth of the activation time
$e.$	Euler's number
$p^{\text{Bound}}, q^{\text{Bound}}$ and r^{Bound}	Coefficients used to define $t_{\text{act}}^{\text{Bound}}$
t	time
$\boldsymbol{D}$	Diffusion tensor
Δ	Laplacian
$\boldsymbol{I}$	Identity matrix
λ_i and Φ_i	Diffusion rate coefficients, where $i = B, C\,or\,F$
α_i	Immature tissue growth rate, where $i = B, C\,or\,F$
β_i	Tissue resorption rate, where $i = B, C\,or\,F$
γ_i	Tissue maturation rate, where $i = B, C\,or\,F$
T_i^G	Immature tissue growth function
T_i^R	Tissue resorption function
T_i^M	Immature to mature tissue maturation function
θ_I and θ_{II}	Direction of the principal stresses
$\otimes$	Tensor product
T_i	Effective range of $t_{\text{act},i}$, where $i = B, C\,or\,F$.
T_i^{Min} and T_i^{Max}	The maximum and minimum values of T_i, where $i = B, C\,or\,F$.
$T_{i,\text{GT}}$	Coefficient used to scale T_i^G where $i = B, C\,or\,F$
$k_i^R, \quad l_i^R$ and m_i^R	Coefficient used to define T_i^R where $i = B, C\,or\,F$
d_i^M, e_i^M and f_i^M	Coefficient used to define T_i^M where $i = B, C\,or\,F$
E_{TOT}	Material Young's modulus
E_i^I	Young's modulus of immature tissues, where $i = B, C\,or\,F$
E_i^M	Young's modulus of mature tissues, where $i = B, C\,or\,F$
E_V	Young's modulus of the free space

1 Introduction

Bone density can evolve in various ways depending on bone growth, healing and remodeling as well as implant osseointegration. While remodeling only involves growth and resorption of bone tissue, other processes can result in the formation of other tissue types, namely cartilage and fibrous tissues. During osteogenesis and fracture healing, the formation of cartilage is observed as a feature of endochondral ossification [15,79,81,89]. Bone, cartilage and fibrous tissue formations may all be observed during bone healing [19,35,51,56,79]. Similarly during implant osseointegration, it has been observed that fibrous tissue may form [29,49,68,72], potentially resulting in the loosening of the prosthesis [77]. The biological phenomena involved in each of these processes can be related through the cellular action driving tissue generation and adaptation. Tissue formation and evolution begins with the migration of Mesenchymal Stem Cells (MSCs) and subsequent differentiation

into tissue-specific cell types. This process of cell differentiation is controlled by several factors including the surrounding mechanical environment which is determined by the geometry and the loading conditions. As the tissue evolves, the mechanics continue to be one of the driving influences on the biological processes and even once homeostasis is achieved. For example in fully formed mature cortical bone, the tissue continues to adapt through the same fundamental cellular processes associated with resorption of bone tissue by osteoclasts and deposition of bone tissue by osteoblast during bone remodeling [17,23,27,88,94]. The contribution of these mechano-biological couplings to the selective evolution of bone tissue, leading to the formation or absence of formation of different tissue types, remains poorly understood. This work proposes to explore this question by means of a multi-tissue model of bone which is intrinsically able to evolve into different tissues.

The mechano-biological processes governing the evolution of osteoarticular tissues, taken separately, have been greatly studied. In particular, the remodeling activity of bone has been shown to be describable by a process, referred to as the mechanostat [31–33,92], involving two competing mechanisms of growth and resorption, both of which are controlled by the local mechanical strains experienced by the tissue. The precise mechanisms and parameters governing the mechanostat have received a lot of attention in recent decades. There is evidence that the initiation and propagation of microdamage in bone is one of the driving factors in initiating and controlling remodeling [4,12,18,64] as this may act as an instigator of osteocyte death, which commences the resorption of damaged bone by osteoclasts and the deposition of new bone tissue by osteoblasts. Furthermore, the ongoing remodeling and refinement of bone structure may be controlled by localized microdamage determining when the time, strain and strain rate-dependent processes of bone resorption, deposition and maturation occur [1,4,12,64]. There exist nowadays a number of models able to describe the evolution and remodeling of bone tissue such as mechano-biological models [7,25,36,37,40,44,46,59,80,84], mechano-biochemical models [2,24,52,53] and models describing the specific cellular processes involved in bone remodeling [55,58,70,78].

In addition to osteogenesis, the formation of cartilaginous and fibrous tissues have also been suggested to follow a similar pattern of strain-induced resorption and growth [31–33]. For these tissues as well, it has been further demonstrated that MSC differentiation and tissue formation is driven by the localized strain conditions [57,71]. The distinction between compressive and tensile loading is proposed to define the strain range where cartilage, bone and fibrous tissues will form [14]. Moreover, the hydrostatic pressure experienced by the material in conjunction with the localized shear strain also influences in determining stem cell differentiation [11,20,57,71].

Current models of fracture healing [11,16,24,41,47,57,71] describe the formation of distinct tissue types in the fracture callus by modeling cellular processes and ECM evolutions; however, they do not predict the evolution of preexisting tissues and the development of newly formed tissues simultaneously within the same formulation. To achieve this, distinct numerical models have been concurrently implemented for bone remodeling and fracture healing regions [35,41,61,93]. These models distinguish between bone remodeling and fracture healing by implementing distinct numerical approaches to each process. A more unified description of tissue evolution in bone able to capture multiple biological processes would allow the simulation of complex situations and anatomical features where several processes can occur in different locations and interact through mechano-biological couplings.

Building upon this evidence for mechanically driven tissue evolution, a model is proposed here to capture the ability of several tissue types to form and interact mechanically with each other depending on the mechanical history. For that, it considers the possibility for different tissue types to grow from dormant populations of MSCs. This model is based on a previous mechano-biological FE model created by Schmitt et al. [82], which has looked at the growth of bone from populations of MSCs to fully formed bone tissue inside titanium scaffolds. In doing so, it has regarded the remodeling process as being driven by a combination of MSC migration, proliferation and maturation and has been able to predict the stiffness of ovine hemimandible bones after three months of remodeling. A modification of this model is proposed here to allow a coupled mechano-biological multi-tissue description of the formation of bone, cartilage and fibrous tissues. To achieve this, a distinction between immature and mature states will be made, which will enable the processes of cellular migration, proliferation and apoptosis and Extra Cellular Matrix (ECM) growth, maturation and resorption to be considered simultaneously.

In Sect. 2 the derivation of the mechanostat model (Sect. 2.2) and the Partial Differential Equations (PDEs) (Sect. 2.3) used in this study are presented. In Sect. 2.4, a description of the input parameters and the FE simulations undertaken to analyze the effectiveness of the model are detailed. In Sect. 3 the results are presented in terms of the model input variables and parameters (Sect. 3.1) and the findings from the FE simulations (Sect. 3.2). Finally, in Sect. 4, a discussion detailing some comparisons with observed remodeling behavior and the model limitations is presented.

2 Methods

2.1 General principle of the model

Three tissue types have been considered: bone, cartilage and fibrous tissue. In the following, only two-dimensional (2D) structures are considered for the sake of simplicity. The spatial distribution of the different tissues within a structure is described by defining the local volume fraction of each tissue. In each given representative volume, the volume fraction occupied by tissues, φ_{TOT}, is defined as

$$\varphi_{\text{TOT}} = \varphi_{B,\text{TOT}} + \varphi_{C,\text{TOT}} + \varphi_{F,\text{TOT}} \tag{1}$$

where $\varphi_{B,\text{TOT}}$, $\varphi_{C,\text{TOT}}$ and $\varphi_{F,\text{TOT}}$ are the volume fractions for bone, cartilage and fibrous tissues, respectively. With this definition, the local volume fraction of unfilled space ("void") is simply given by: $\varphi_V = 1 - \varphi_{\text{TOT}}$ and the value of φ_{TOT} cannot exceed 1, when the whole volume is occupied by tissue.

To model the distinct cellular, biological and mechanical behaviors observed during tissue evolution, each tissue is considered to exist in two possible states referred to as immature and mature (Fig. 1). The immature state describes the tissue in the early stages of formation as a cluster of cells. Through the effects of the cellular processes of migration, proliferation and apoptosis, and the preliminary stages of ECM formation, the evolution of tissues in the immature state is described. Mature tissue results only from the maturation of immature tissue which reflects the consolidation of the ECM and embedding of cells in it, as such, tissues in mature state cannot
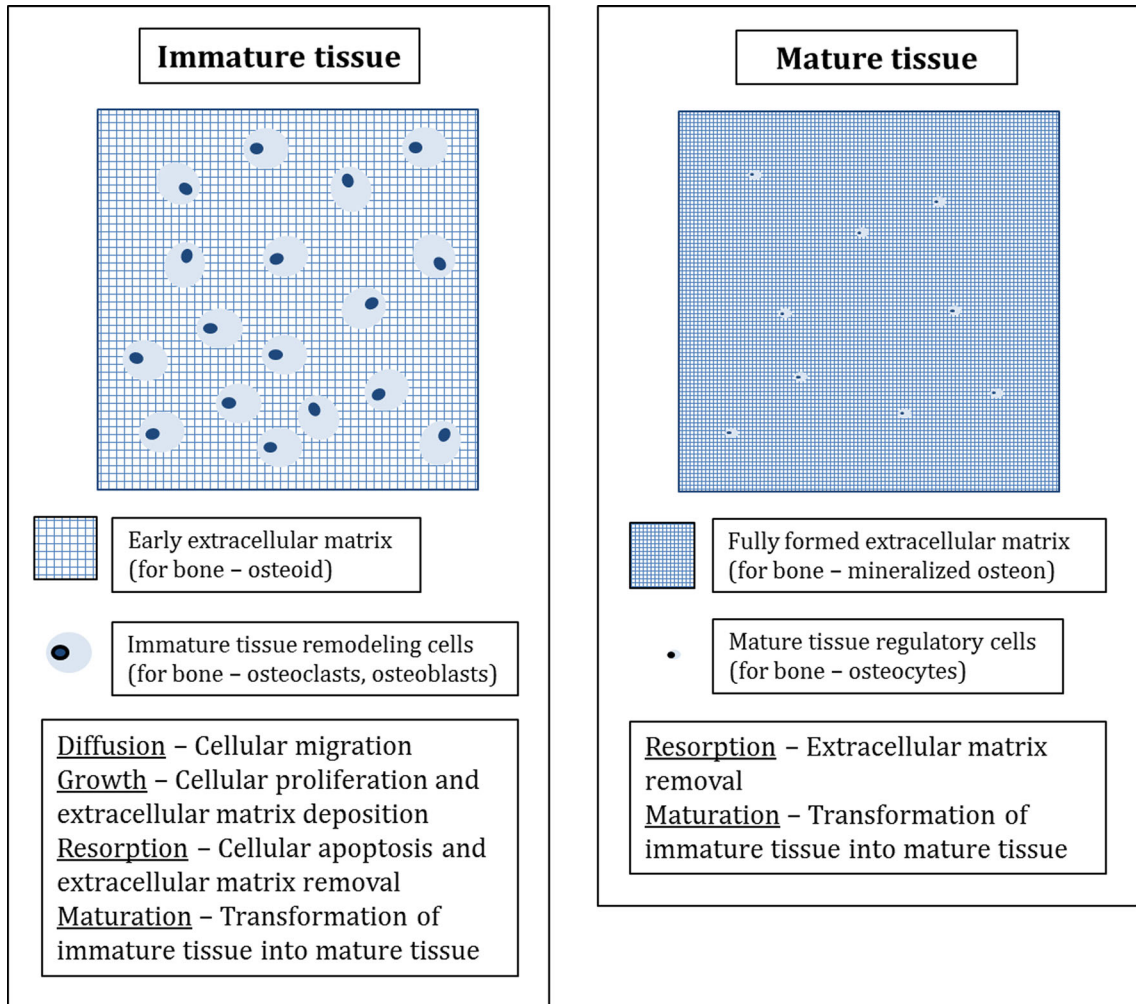

Fig. 1 Schematic representation of the distinction between immature and mature tissue states
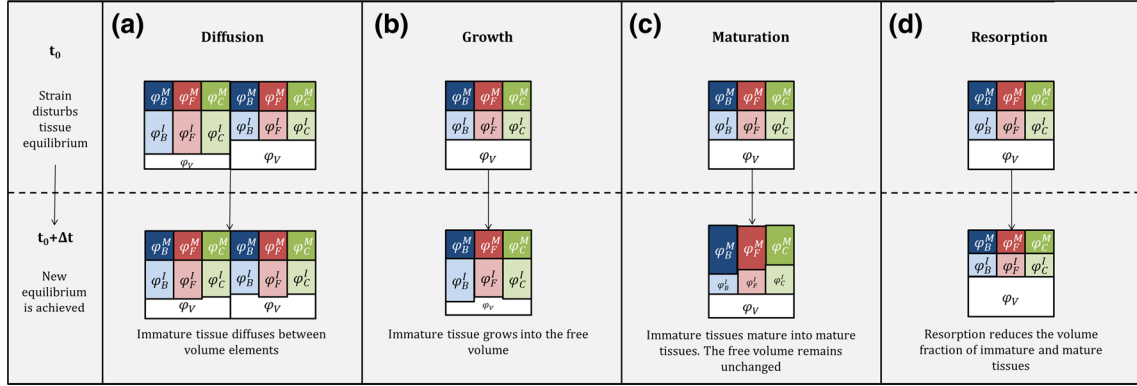
Fig. 2 Schematic representation of the different remodeling processes involved in the mechanostat: diffusion (**a**), growth (**b**), maturation (**c**) and resorption (**d**)

diffuse nor grow but can be resorbed. In the particular case of bone tissue, the distinction between immature and mature tissue provides a way to capture the processes of primary and secondary mineralization [1,4,64]. Therefore, for each tissue type, the volume fraction $\varphi_{i,\text{TOT}}$ where $i = B, C, F$ is decomposed as the sum of the volume fractions of immature (φ_i^I) and mature (φ_i^M.) tissues:

$$\varphi_{i,\text{TOT}} = \varphi_i^I + \varphi_i^M \tag{2}$$

The chart shown in Fig. 2 illustrates the different processes through which the composition of a representative volume element can evolve under loading. The volume fractions of immature tissue, mature tissue and free space are represented as areas within a representative volume element of the tissue. For illustrative purpose, the tissue volume fractions are depicted as being in separate distinct regions of the material, but in the model each tissue will be distributed evenly at the scale of this representative volume. This continuum description suggests a limit in the spatial resolution of the model, which should be of the order of a characteristic tissue microscopic feature, typically, the size of an osteon for bone ($\sim 300\mu$m). The link between mechanics and biology may no longer be sufficient to accurately describe tissue evolutions below this length scale as (i) further molecular and chemical factors should be taken into account together with the mechanical environment and (ii) more complex features would need to be considered like the vascular and nerves networks.

In the proposed description, the evolution of tissue composition and organization is driven by the local strain environment. At a given time t_0, tissues of different types (B, C, F) and in different states (M, I) occupy given volume fractions. In Fig. 2, the initial composition corresponds to one-third of immature tissue, one-third of mature tissue, one-third of free space, with equal repartition of bone, cartilage and fibrous tissues. As a loading is applied to the volume, the strain is altered and this defines how the immature and mature tissues will respond. At time $t_0 + \Delta t$, a new composition is achieved where the volume fractions of each tissue type and the free space have been altered due to different possible processes. For a given immature tissue type, diffusion through cellular migration can occur if there is a gradient in immature tissue composition between two elements (Fig. 2a). If the strain state is favorable, mature and immature tissues can grow and generate more immature tissue (Fig. 2b). If an appropriate level of strain is maintained for some time, immature tissues can become mature tissues (Fig. 2c). Conversely, if the strain is no longer in the range where growth occurs, then resorption will begin: mature and immature tissue volume fractions will decrease (Fig. 2d). In Fig. 2, all three tissue types ($B, C,$ and F) evolve following the same processes; however, the response to strain history in terms of growth, diffusion, resorption and maturation is unique for each tissue type.

All the processes shown in Fig. 2 will affect the local Young's modulus to a certain degree due to the change in volume fractions, but most notably the Young's modulus is going to be influenced by the fluctuations in mature tissue content because the Young's modulus of mature tissue, especially bone, is significantly higher. This local change in mechanical properties will in turn modify the stress and strain distributions in the tissue. Immature tissue will continue to grow and mature until the Young's modulus has increased to a level where the strain is no longer in the range where growth or maturation may occur. As a result of these processes, it is expected that for a given loading, a balance between growth, maturation and resorption should establish, corresponding to the mechanostat.

2.2 Modeling of the mechanostat

In order to model the mechanostat, a measure of the accumulated strain over time is required to define the strain sensitivity of tissue growth, maturation and resorption. For that, the first (ε_I.) and the second (ε_{II}) principal strains in the tissue are normalized with respect to the yield strain ε_Y of cortical bone ([6,95]). The normalized strains along the principal directions $\varepsilon_{k,N}$ are then defined as:

$$\varepsilon_{k,N} = \frac{\varepsilon_k}{\varepsilon_Y} \tag{3}$$

where subscript k = (I or II) refers to normalized strain in the principal directions I and II, respectively. The principal strains have been normalized in this manner to define a tailorable strain region in the global material where tissue growth is likely to occur, be relatable to the global tissue properties and act as a relative measure of tissue damage. This normalization also provides a means to account for the variability of the yield strain with the strain rate in future models.

For bone (B) tissue, both the first and second principal strains are considered because bone tissue is generally observed to grow when loaded under both positive and negative strains [20]. Cartilage (C) and fibrous (F) tissues, however, are only sensitive to the second and first principal strains, respectively [14,20]. Accordingly, we define tissue-specific functions, $f_{i,k}\left(\varepsilon_{k,N}\right)$ for each tissue type i, as follows:

$$f_{i,k}\left(\left|\varepsilon_{k,N}\right|\right) = a_{i,k}^{\varepsilon}\left|\varepsilon_{k,N}^2\right| + b_{i,k}^{\varepsilon}\left|\varepsilon_{k,N}\right| + c_{i,k}^{\varepsilon} \tag{4}$$

where $a_{i,k}^{\varepsilon}$, $b_{i,k}^{\varepsilon}$ and $c_{i,k}^{\varepsilon}$ are characteristic coefficients for each tissue type and $|.|$ is the absolute value. This produces a parabolic function describing the evolution of accumulated strain as a function of the current absolute value of the normalized principal strains. As a consequence of the parabolic function, there is no 'lazy zone' included in this mechanostat model. The absolute values of the principal strains are used in this expression so that there is no distinction made between positive and negative values of principal strains on the change in accumulated strain. For bone, both $f_{B,I}\left(\left|\varepsilon_{I,N}\right|\right)$ and $f_{B,II}\left(\left|\varepsilon_{II,N}\right|\right)$ are needed to describe bone tissue evolution in tension and compression [19,67,91] while for cartilage and fibrous tissue, only $f_{C,II}\left(\left|\varepsilon_{II,N}\right|\right)$ and $f_{F,I}\left(\left|\varepsilon_{I,N}\right|\right)$ are used [13,14].

For each tissue type, the accumulation of strain over time is described by a time integral of strain, denoted $t_{\mathrm{act},i}$. It is calculated using the corresponding functions $f_{i,k}\left(\left|\varepsilon_{k,N}\right|\right)$, as follows:

$$\frac{\partial t_{\mathrm{act},i}}{\partial t} = f_{i,k}\left(\left|\varepsilon_{k,N}\right|\right)\left(t_{\mathrm{act},i}^{\mathrm{Bound}}\right) \tag{5}$$

where t is the time, $t_{\mathrm{act},i}^{\mathrm{Bound}}$ is a function used to control the rate of change of $t_{act,i}$. For bone tissue, $t_{act,B}$ is generated from the sum of $f_{B,I}\left(\left|\varepsilon_{I,N}\right|\right)$ and $f_{B,II}\left(\left|\varepsilon_{II,N}\right|\right)$. To ensure $t_{\mathrm{act},i}$ remains responsive to changing strain conditions in the tissue, a Gaussian distribution $t_{\mathrm{act},i}^{\mathrm{Bound}}$ has been used. This ensures that the rate of change of $t_{\mathrm{act},i}$ does not increase (resp. decrease) excessively rapidly in over (resp. under) strained regions.

$$t_{\mathrm{act},i}^{\mathrm{Bound}} = p_i^{\mathrm{Bound}} e^{\left[\frac{(t_{\mathrm{act},i} - q_i^{\mathrm{Bound}})^2}{2 r_i^{\mathrm{Bound}\,2}}\right]} \tag{6}$$

where p_i^{Bound}, q_i^{Bound} and r_i^{Bound} are coefficients specific for each tissue type.

For a given tissue i, the sign and value of the cumulated strain $t_{\mathrm{act},i}$ are used to model the activation and the rates of resorption, growth and maturation. Where the normalized strain, $\varepsilon_{k,N}$, produces a negative value for the expression $f_{i,k}\left(\left|\varepsilon_{k,N}\right|\right)$, the value of $t_{\mathrm{act},i}$ will decrease. If $t_{\mathrm{act},i}$ becomes negative, tissue is resorbed. Conversely, where $\varepsilon_{k,N}$ produces a positive value for the expression $f_{i,k}\left(\left|\varepsilon_{k,N}\right|\right)$ then the value of $t_{\mathrm{act},i}$ will increase. As $t_{\mathrm{act},i}$ becomes positive, this causes growth and maturation.

This description is refined by introducing another tissue-specific variable T_i to define an effective range of $t_{\mathrm{act},i}$ values so that the tissue growth and resorption rates are limited by a maximum and minimum permissible value. Under situations where $t_{\mathrm{act},i}$ increases (resp. decreases) rapidly, the rate of tissue growth or resorption is maintained at realistic values until $t_{\mathrm{act},i}$ decreases (resp. increases) within a certain range of T_i again. This variable T_i is expressed as

$$T_i = \begin{cases} T_i^{\mathrm{Min}} \ when \ t_{\mathrm{act},i} < T_i^{\mathrm{Min}} \\ t_{\mathrm{act},i} \ when \ T_i^{\mathrm{Min}} < t_{\mathrm{act},i} < T_i^{\mathrm{Max}} \\ T_i^{\mathrm{Max}} \ when \ t_{\mathrm{act},i} > T_i^{\mathrm{Max}} \end{cases} \tag{7}$$

where T_i^{Min} and T_i^{Max} are the minimum and maximum values of T_i.

For each tissue type, growth, resorption and maturation occur for different ranges of accumulated strain. This is modeled through different functions T_i^G, T_i^R and T_i^M setting the range of T_i over which growth, resorption and maturation occur, respectively. They are defined as follows:

$$T_i^G = \begin{cases} \frac{T_i}{T_{i,\,GT}} \ when \ T_i > 0 \\ 0 \ when \ T_i \leq 0 \end{cases} \tag{8}$$

$$T_i^R = k_i^R e^{\left[\frac{(T_i - l_i^R)^2}{2m_i^{R2}} \right]} \tag{9}$$

$$T_i^M = d_i^M e^{\left[\frac{(T_i - l_i^M)^2}{2m_i^{M2}} \right]} \tag{10}$$

For growth, T_i^G is zero when T_i is negative and scales as the value of $T_{i,\mathrm{GT}}$ linearly when T_i is positive. This ensures that immature tissue growth occurs progressively more rapidly as T_i increases, replicating the time lag during bone tissue primary mineralization [4,64]. Likewise, T_i^R and T_i^M are Gaussian distributions which scale the value of T_i to replicate the rate and strain range for tissue resorption and maturation. The parameters k_i^R, l_i^R and m_i^R, and d_i^M, e_i^M and f_i^M are tissue-specific coefficients of resorption and maturation, respectively.

As an illustration, Fig. 3 shows a hypothetical evolution of the cumulated strain variables $t_{\mathrm{act},i}$ (Fig. 3a) and T_i (Fig. 3b) as time progresses and as the strain within the tissue changes. At the beginning (step 1), strain is applied to the tissue causing $t_{\mathrm{act},i}$ to increase. As a result, the growth of immature tissue is initiated with an increasing rate scaling T_i^G (Fig. 3c) and maturation of this tissue may also start with an increasing rate scaling T_i^M (Fig. 3d). At some point (step 2), cumulated strain exceeds a tissue-specific threshold: $t_{\mathrm{act},i}$ grows larger than T_i^{Max} and the upper threshold for T_i is reached. As long as $t_{\mathrm{act},i}$ is greater than T_i^{Max}, the rates of growth and maturation will saturate. Under the effect of maturation, the tissue gets stiffer and the cumulated strain is reduced to a level where $t_{\mathrm{act},i}$ begins to decrease (step 3). As $t_{\mathrm{act},i}$ continues to fall below T_i^{Max} (step 4), the rate of growth and maturation decrease, as shown in Figure 3c and d. At some point (step 5), $t_{\mathrm{act},i}$ falls below zero. Growth and maturation reduce to almost zero while tissue resorption begins to dominate with a rate scaling as T_i^R (Fig. 3e). When $t_{\mathrm{act},i}$ drops below T_i^{Min} (step 6), the lower threshold for T_i is reached. Consequently, the rate of resorption saturates. As the tissue resorbs, the strain increases again (step 7) and rises above T_i^{Min}, therefore slowing down the resorption process (step 8).

2.3 PDFS for immature and mature tissue development

The evolution of immature tissues is described by four specific terms: diffusion, growth, resorption and maturation describing the migration, the proliferation, the apoptosis of cells and the transformation of immature tissue into the mature state after a maturation period, respectively. One diffusion–reaction equation for each tissue type i describes these processes as follows:

$$\frac{\partial \varphi_i^I}{\partial t} = \overbrace{(1 - \varphi_{TOT}) \boldsymbol{D}_i \Delta \varphi_i^I}^{\text{Diffusion}} + \overbrace{\alpha_i (1 - \varphi_{TOT}) \varphi_{TOT} \left(T_i^G \right)}^{\text{Growth}} - \overbrace{\beta_i \varphi_i^I \left(T_i^R \right)}^{\text{Resorption}} - \overbrace{\gamma_i \varphi_i^I \left(T_i^M \right)}^{\text{Maturation}} \tag{11}$$

For diffusion, the tissue-specific diffusion tensor $\boldsymbol{D}_i$ reads

$$\boldsymbol{D}_i = \lambda_i \boldsymbol{I} + \Phi_i \left(\sqrt{|\varepsilon_I|} \theta_I \otimes \theta_I + \sqrt{|\varepsilon_{II}|} \theta_{II} \otimes \theta_{II} \right) \tag{12}$$
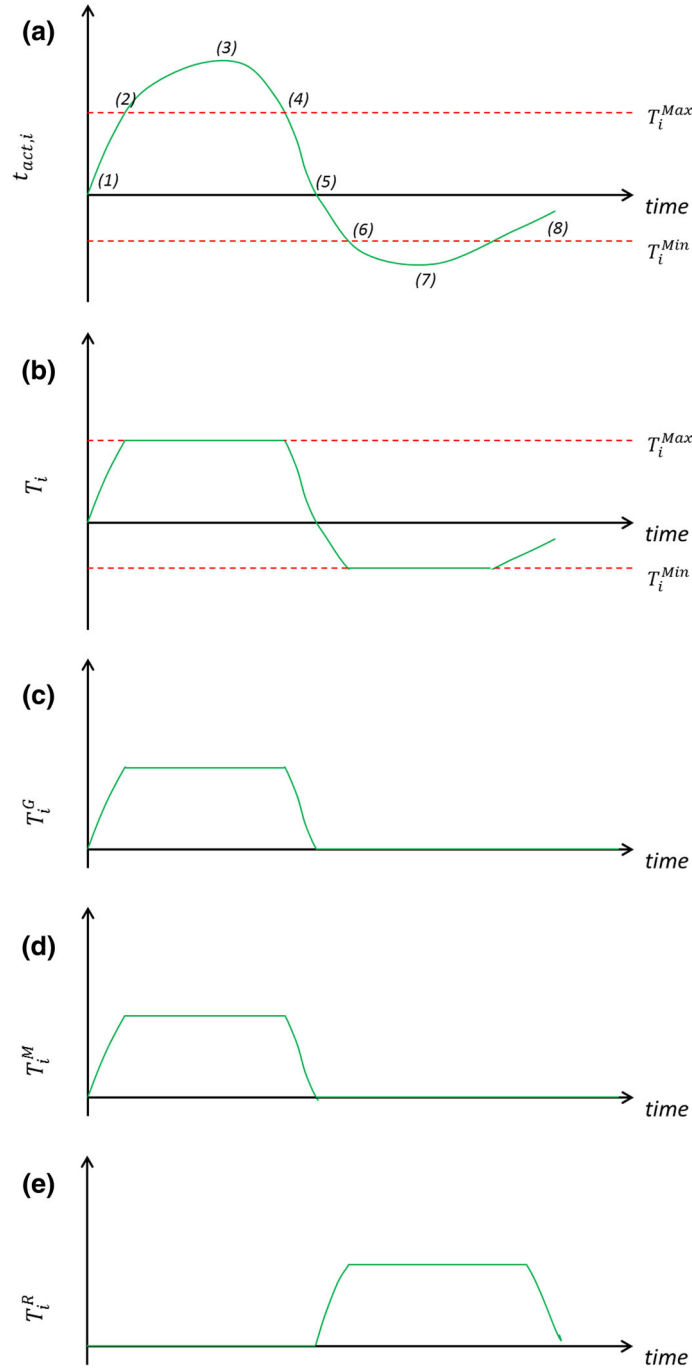
Fig. 3 Example graph of the time evolution of **a** $t_{\text{act},i}$ **b** T_i **c** T_i^G **d** T_i^M **e** T_i^R to the changing mechanical environment

where λ_i and Φ_i are tissue-specific constants, I is the identity matrix, θ_I and θ_{II} are the directions of the principal stresses and $\otimes$ represents the tensor product. The corrective factor $(1 - \varphi_{\text{TOT}})$ accounts for the fact that diffusion can only take place in the remaining unfilled volume fraction.

For growth, it is considered that all tissue types can generate new immature tissue of any type. For this reason, this contribution scales as φ_{TOT} with a specific growth rate coefficient α_i. As is the case for diffusion, the corrective factor $(1 - \varphi_{\text{TOT}})$ accounts for the fact that growth can only take place in the remaining unfilled volume fraction. Resorption and maturation both lead to a decrease in immature tissue content. They simply scale as φ_i^I with rate coefficients β_i and γ_i for resorption and maturation, respectively.

Similarly, the evolution of mature tissue is defined by a reaction equation for each tissue type as follows:

$$\frac{\partial \varphi_i^M}{\partial t} = \overbrace{\gamma_i \varphi_i^I \left(T_i^M \right)}^{\text{Maturation}} - \overbrace{\beta_i \varphi_i^M \left(T_i^R \right)}^{\text{Resorption}} \tag{13}$$

In these equations, the first term of the sum corresponds to the contribution of the maturation process and therefore scales as $\gamma_i \varphi_i^I$. The second term corresponds to the resorption process, which scales as $\beta_i \varphi_i^M$, assuming that resorption of mature and immature tissues has the same rate coefficients β_i.

Hooke's law was used to provide a linear isotropic elastic relationship between stress and strain, and mechanical equilibrium is achieved by:

$$\mathbf{Div}\,\sigma + f = 0 \tag{14}$$

where σ is the Cauchy's stress tensor and f is the body loads.

Finally, to combine the linear elastic isotropic material models applied to each tissue type, in both the immature and mature state, a simple composite description has been chosen for the local Young's modulus volume element, E_{TOT} which reads:

$$E_{\text{TOT}} = \varphi_B^I E_B^I + \varphi_B^M E_B^M + \varphi_C^I E_C^I + \varphi_C^M E_C^M + \varphi_F^I E_F^I + \varphi_F^M E_F^M + \varphi_V E_V \tag{15}$$

where E_i^I and E_i^M are the Young's moduli of the immature and mature tissue components, respectively, and E_V is the Young's modulus of free space which is set to zero. Here, the same value for the Poisson's ratio was chosen for all tissue types. For all the above equations, a zero flux boundary condition is applied on free surfaces.

2.4 FE simulations

A 2D planar FE model was created using COMSOL Multiphysics® software version 4.4. The geometry of interest was a cantilever beam with dimensions 250 mm in length and 30 mm in depth corresponding approximately to half a femur shaft, as shown in Fig. 4. All nodes on the left edge of the beam were completely fixed in all degrees of freedom. The Poisson's ratio and the density were set to 0.3 and 2000 kg/m^3, respectively, for each tissue. The mesh for each simulation was generated using low-order quadratic triangular elements to improve computational efficiency and the system was solved using an implicit solver with a convergence tolerance factor of 1E−10. A mesh convergence analysis was carried out with the defining convergence quantities being the fraction of mature bone tissue averaged over the entire beam for *Simulations 1* and 3 and fraction of mature cartilage tissue averaged in the upper void for *Simulation 2*. The convergence criteria were defined as a change in φ_B^M or φ_C^M of < 1% in the region of interest between mesh refinements. The mesh convergence analysis is shown in "Appendix A.1".

Three simulations were chosen to identify the tissue evolutions under different loading conditions and initial tissue volume fractions as detailed in Table 1. *Simulation 1* applied a static pressure load (2.5 MPa) distributed vertically at the free end (right side) of the specimen. This simulation was intended to replicate the initial tissue distributions and loading of a mid-diaphysis section of a long bone. Correspondingly, three longitudinal regions, each 0.01 m in depth, were defined (Fig. 4a). The upper and lower surface regions were initially set to have volume fractions of predominantly mature bone ($\varphi_B^I = 0.05$, $\varphi_B^M = 0.85$, $\varphi_V = 0.06$ and $\varphi_C^I = \varphi_F^I = \varphi_C^M = \varphi_F^M = 0.01$) to replicate the cortical shell of a mid-diaphysis long bone, and the central core region was initially defined to be a mixture of immature tissues ($\varphi_B^M = 0.05$, $\varphi_C^M = \varphi_F^M = 0.01$, $\varphi_B^I = \varphi_C^I = \varphi_F^I = 0.2$ and $\phi_V = 0.33$). *Simulation 2* looked at the scenario where there were initially two voids in the beam positioned near the fixed left side (Fig. 4b) the initial volume fractions of the specimen were defined to be predominantly mature bone ($\varphi_B^I = 0.05$, $\varphi_B^M = 0.85$, $\varphi_V = 0.06$ and $\varphi_C^I = \varphi_F^I = \varphi_C^M = \varphi_F^M = 0.01$) and within the voids to be zero. The loading applied to *Simulation 2* was again static pressure load (2.5 MPa) distributed vertically on the free end. This simulation was intend to investigate how the mature bone content would adapt or remodel over time and which tissue types would form in the two voids replicating a bone growth or fracture healing scenario. Finally, *Simulation 3* divided the specimen into two distinct longitudinal regions with predominantly mature bone ($\varphi_B^I = 0.05$, $\varphi_B^M = 0.85$, $\varphi_V = 0.06$ and $\varphi_C^I = \varphi_F^I = \varphi_C^M = \varphi_F^M = 0.01$) in the upper region and immature tissues ($\varphi_B^M = 0.05$, $\varphi_C^M = \varphi_F^M = 0.01$, $\varphi_B^I = \varphi_C^I = \varphi_F^I = 0.2$ and $\varphi_V = 0.33$)
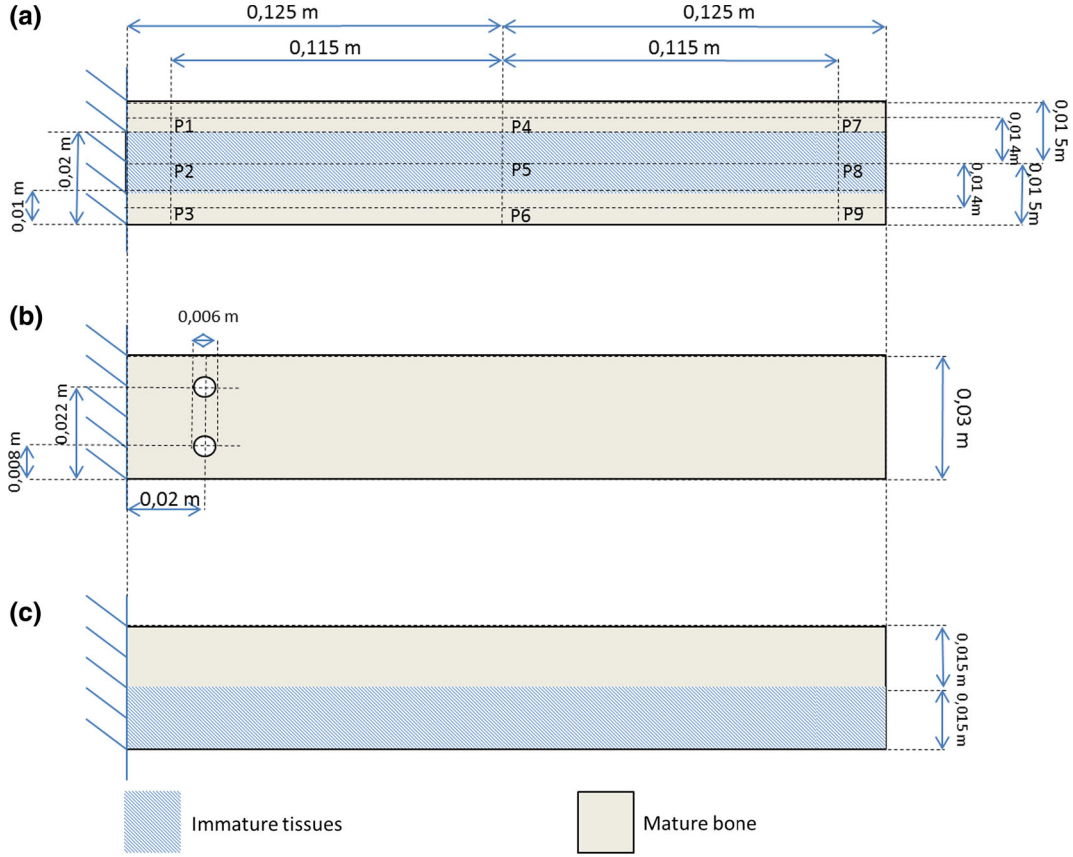
Fig. 4 FE cantilever beam used in *Simulations 1–3* and the measurement grid (point P1–P9). Beam **a** was used in *Simulations 1*, beam **b** used in *Simulation 2* and beam **c** used in *Simulation 3*. All dimensions are in meters

in the lower region (Fig. 4c). A vertically distributed cyclic loading was applied ($\sin\left(\frac{\pi t}{36,000}\right)$ MPa). This simulation was intended to investigate the tissue formations in the lower half of the specimen and bone tissue evolution in the upper section.

Simulation 1 was simulated for a period of 10,000 h and *Simulations 2* and 3 were simulated for a shorter period of 1000 h. Plots of $\varepsilon_{k,N}$, φ_i^I and φ_i^M from all three simulations were taken at nine points P1–9, as shown in Fig. 4. A complete list of the input variables for all simulations is given in Table 2.

3 Results

3.1 Mechanostat model variables and parameters

An important aspect of this model is the justification for the input variables and parameters of the model. The following section explains the rationale behind the choice of these values and how they have been determined.

Figure 5 shows the curves $f_{i,k}\left(\varepsilon_{k,N}\right)$ used to define the growth and resorption for each tissue type with respect to the localized strain in the material. Each curve is a parabola defined by the coefficients $a_{i,k}^{\varepsilon}$, $b_{i,k}^{\varepsilon}$ and $c_{i,k}^{\varepsilon}$. These coefficients have been chosen in order to provide the x-axis intersect and height of the curves at the desired strain regions for each tissue. To produce a positive change in $t_{\text{act},i}$ each tissue needs to be within a specific range of $\varepsilon_{k,N}$. In the following, a value for the yield strain $\varepsilon_Y = 0.006$ [6] has been used to normalize the strain. For bone tissue, a lower strain threshold below which no bone growth occurs has been suggested to be of the order of $\varepsilon = 0.0014$ [32,33], which corresponds to a normalized strain threshold of approximately 0.23. In this model, a slightly lower normalized strain value of 0.16 was used to account for the influence of strain rate dependence on the yield strain which may result in remodeling being initiated at lower strains [73,95,96]. The upper strain limit of bone growth was chosen to be around the yield strain ($\varepsilon_{k,N} = 1$) because around
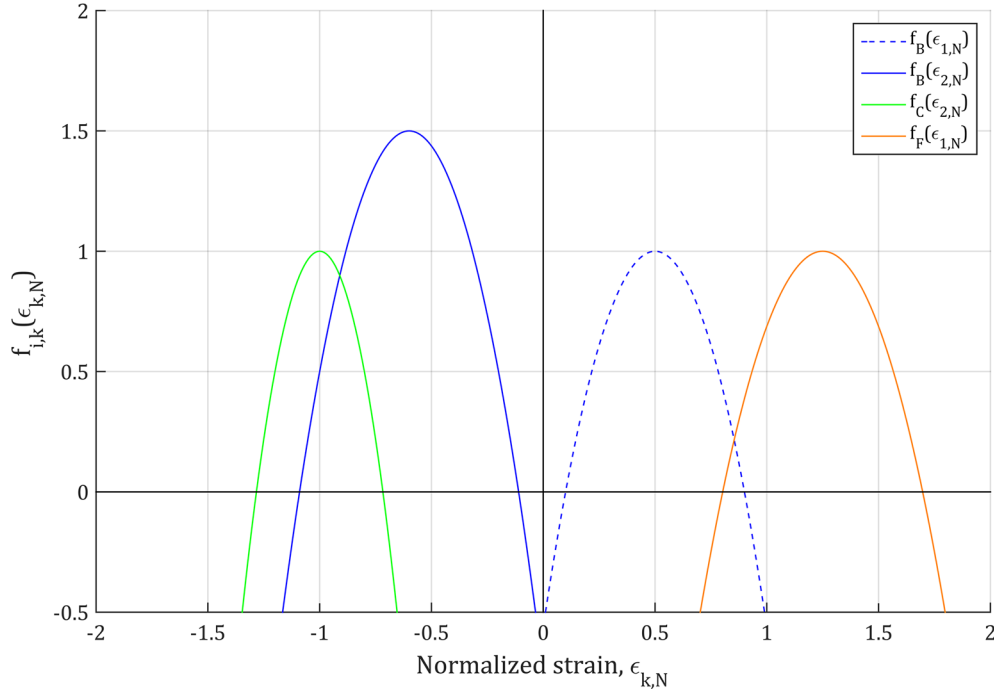
Fig. 5 Plots of $f_{i,k}\left(\varepsilon_{k,N}\right)$ for each tissue. Bone (blue dashed—first principal strain), (blue solid—second principal strain); Cartilage (green—second principal strain) and Fibrous (orange—first principal strain)

this point the bone tissue begins to experience permanent microdamage which would result in localized tissue resorption [73,95,96]. The upper strain threshold for bone tissue remodeling was chosen to be 15% higher than the yield strain for compression ($\varepsilon_{II,N} = 1.15$) and 15% lower than the yield strain for tension ($\varepsilon_{I,N} = 0.85$). This distinction was made to account for the greater toughness and yield point in bone under compression [6,21]. Therefore for bone, first principal normalized strains in the range $0.16 < \varepsilon_{I,N} < 0.85$ (Fig. 5, blue dashed curve) and second principal normalized strains in the range $-0.16 < \varepsilon_{II,N} < -1.15$ (Figure 5, blue solid curve) prompt $t_{\mathrm{act},i}$ to increase thus encouraging localized bone growth.

Likewise, for cartilage and fibrous tissue the lower remodeling threshold has been suggested to be in the region of $\varepsilon = 0.004$ [32,33] which implies a normalized strain of approximately 0.7. For strains significantly higher than the yield point of cortical bone, all tissue types are likely to experience failure. Consequently, resorption was assumed to dominate for all tissues beyond this point, namely in the region of $|\varepsilon_{k,N}| > 1.7$. It has been observed further that cartilaginous and fibrous tissues form at higher strain levels than bone tissue [14,20,32,33,71] and that the upper threshold for growth of cartilaginous tissue is likely to be lower than for fibrous tissue [20]. For this reason, the curves describing the remodeling of cartilage and fibrous tissues were positioned at higher strain regions than those of bone, but with the curve for cartilage having a lower upper limit of $\varepsilon_{k,N} = -1.3$. Therefore, the range of normalized strain values used to define the growth of cartilage tissue was set to $-0.7 < \varepsilon_{II,N} < -1.3$ (Fig. 5, green curve) where the second principal strain was used to describe the growth of cartilage in compression rather than tension ([14]). For fibrous tissue, the range of normalized strain was set to $0.7 < \varepsilon_{I,N} < 1.7$ (Fig. 5, orange curve) where the first principal strain was used to describe fibrous growth predominantly in tension.

The parameter values used for $f_{i,k}\left(\varepsilon_{k,N}\right)$ define the strain ranges over which growth, maturation and resorption occur. When the strain is within the range where $f_{i,k}\left(\varepsilon_{k,N}\right) > 0$, $t_{\mathrm{act},i}$ increases and thus, both growth and maturation will begin. Conversely, when the strain is outside this range $f_{i,k}\left(\varepsilon_{k,N}\right) < 0$, resorption will dominate. The sensitivity to accumulated strain for each process and each tissue is represented in Fig. 6 using the set of parameters listed in Table 2. These curves show the rate of change of the immature tissue growth T_i^G, tissue resorption T_i^R, and maturation T_i^M for each tissue type over the range $-5h < T_i < 15h$. The growth, maturation and resorption rates were chosen from observed literature of fibrous, cartilage and bone tissue development [4,14,20,42,64,81].
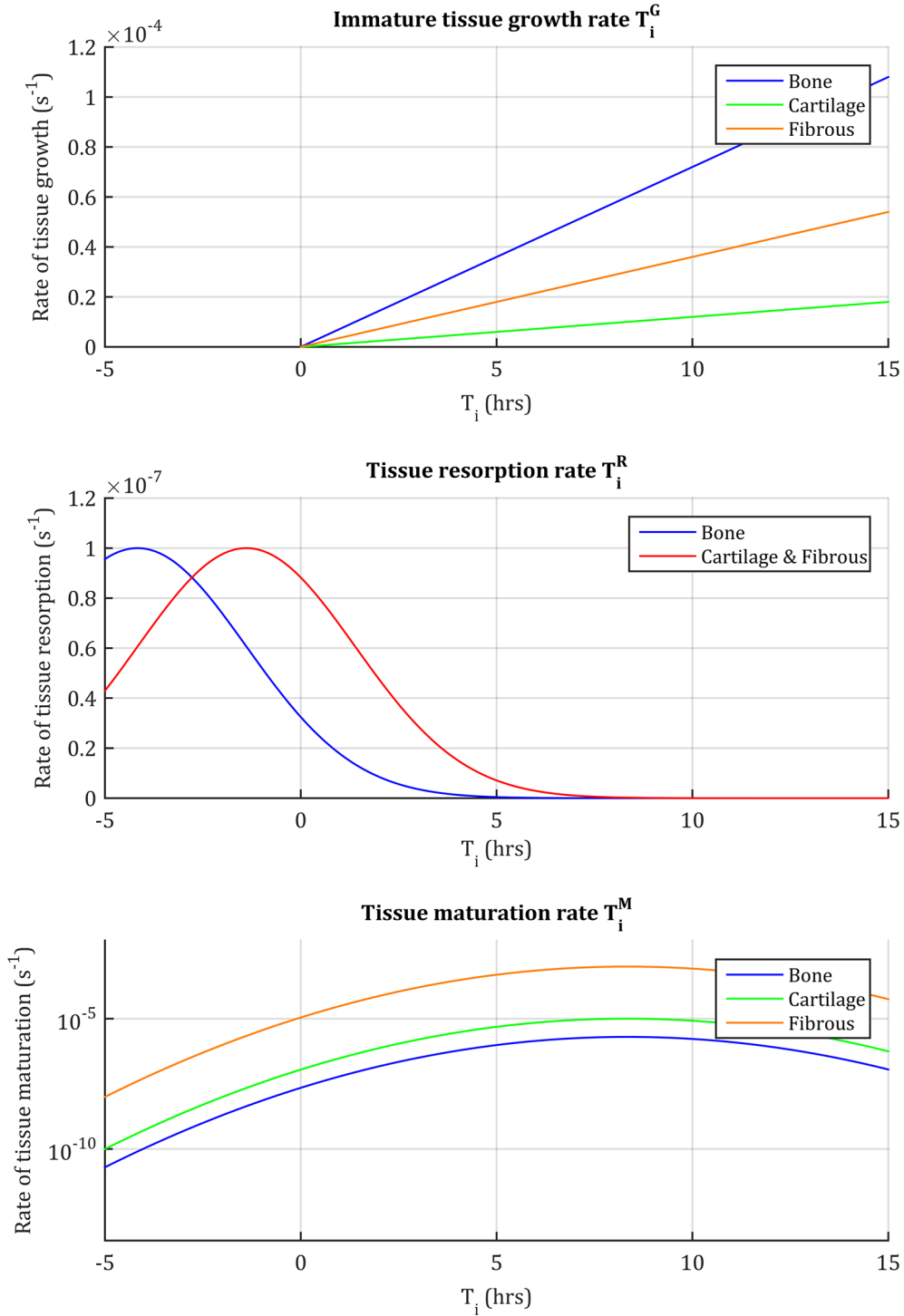
Fig. 6 Plots of the immature tissue growth rate T_i^G resorption rate T_i^R and maturation rate T_i^M. Note that the resorption rates for cartilage and fibrous tissues are the same

3.2 FEA

The following section will detail the results from *Simulations 1 to 3* which investigated a statically loaded specimen replicating the 2D geometry of a mid-diaphysis section of a long bone (*Simulation 1*), a statically
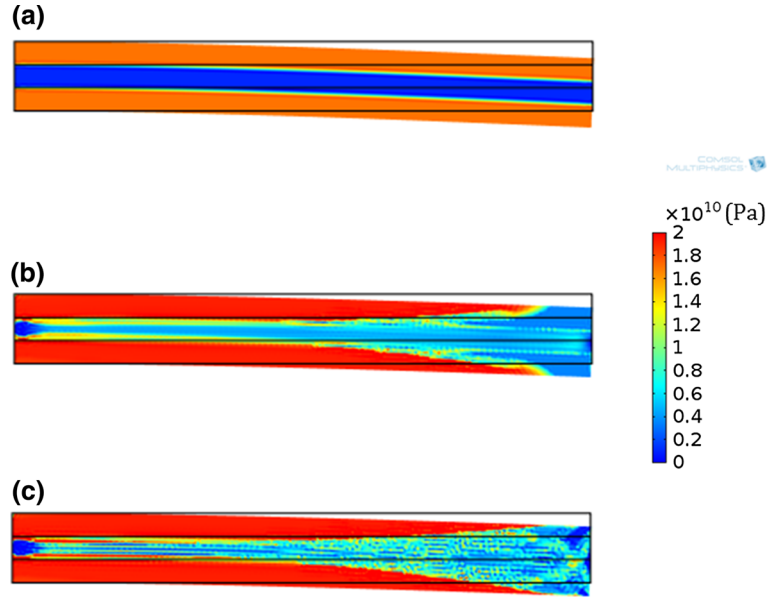
Fig. 7 The Young's modulus after 0, 5000 and 10,000 h across the specimen in *Simulation 1*

loaded specimen with voids (*Simulation 2*) and a specimen with two distinct regions of different initial volume fractions (*Simulation 3*). The specific and complete results for each simulation are reported in "Appendix Sections A.2, A.3 and A.4".

Figure 7 shows the change in Young's modulus across the specimen in *Simulation 1* after 0, 5000 and 10,000 h; it can be observed that where there is initially two distinct regions of cortical bone at the start of the simulation these have adapted to the stress conditions generated by the loading environment to adapt the structure and after 10,000 h there is a region similar to cancellous bone which has formed along the center of the specimen toward the free end (Fig. 7c). Figure 8 shows the tissue evolution for total (8a), bone (8b), cartilage (8c) and fibrous (8d) tissue volume fractions averaged across the entire specimen during the 10,000 h of simulated time for *Simulation 1*. It can be seen that there is an increase in mature bone tissue from the initial conditions of $\varphi_B^M = 0.6$ to $\varphi_B^M = 0.7$ over the course of the simulation and that a steady state is reached for total tissue content. Bone tissue further shows an initial increase in φ_B^I during the initial 500 h followed by a decrease which corresponds to the maturation of bone tissue during the early stages of the simulation (first 2000 h). For cartilage and fibrous tissues, both the immature and mature tissue contents decrease during the simulation. This is because the maximum normalized strain produced during *Simulation 1* ($\varepsilon_{k,N} = 0.6$) remains below the lower strain threshold required for cartilage and fibrous tissue growth ($\varepsilon_{k,N} = 0.7$), as can be seen in Figs. 19 and 20.

Figure 8 gives global evolutions averaged over the whole beam. A more detailed picture of the local variations is given in *Video 1* where the evolution of Young's modulus over the 10,000 h period of the simulation is shown. *Videos 2* and 3 show the evolution of mature and immature bone tissue over the 10,000 h period. The local evolution was also studied by following the changes in tissue composition and properties in different points of the specimen (P1 and P9). Hereafter, points P1 ($x = 0.01$ m, $y = 0.025$ m) and P9 ($x = 0.125$ m, $y = 0.005$ m) are discussed in more detail as they represent the most relevant and interesting cases of growth and resorption during *Simulation 1*. P1 is near the upper surface next to the fixed corner and P9 is near the lower surface at the free end of the specimen (Fig. 4).

Figure 9 shows the evolution at P1 and P9 during *Simulation 1* of the normalized principal strains Fig. 9a, b, the activation cumulated strain for bone tissue T_B Fig. 9c, d, the Young's modulus E_{TOT} Fig. 9e, f and the volume fractions of immature and mature bone, cartilage and fibrous tissues Fig. 9g, l. As expected for bending, the initial tensile strain at point P1 is higher than the compressive strain (Fig. 9a), while the inverse occurs on the lower surface at point P9 (Fig. 9b), this region of the specimen is initially relatively under strained and therefore there is no significant strain observed at point P9 during the initial 3000 h of the simulation. The initial normalized strain values at P1 (0.25–0.6) cause the value of T_B to increase rapidly to its maximum value (50,000 s) (Fig. 9c). This increase in T_B induces the immature bone tissue to grow and mature into mature
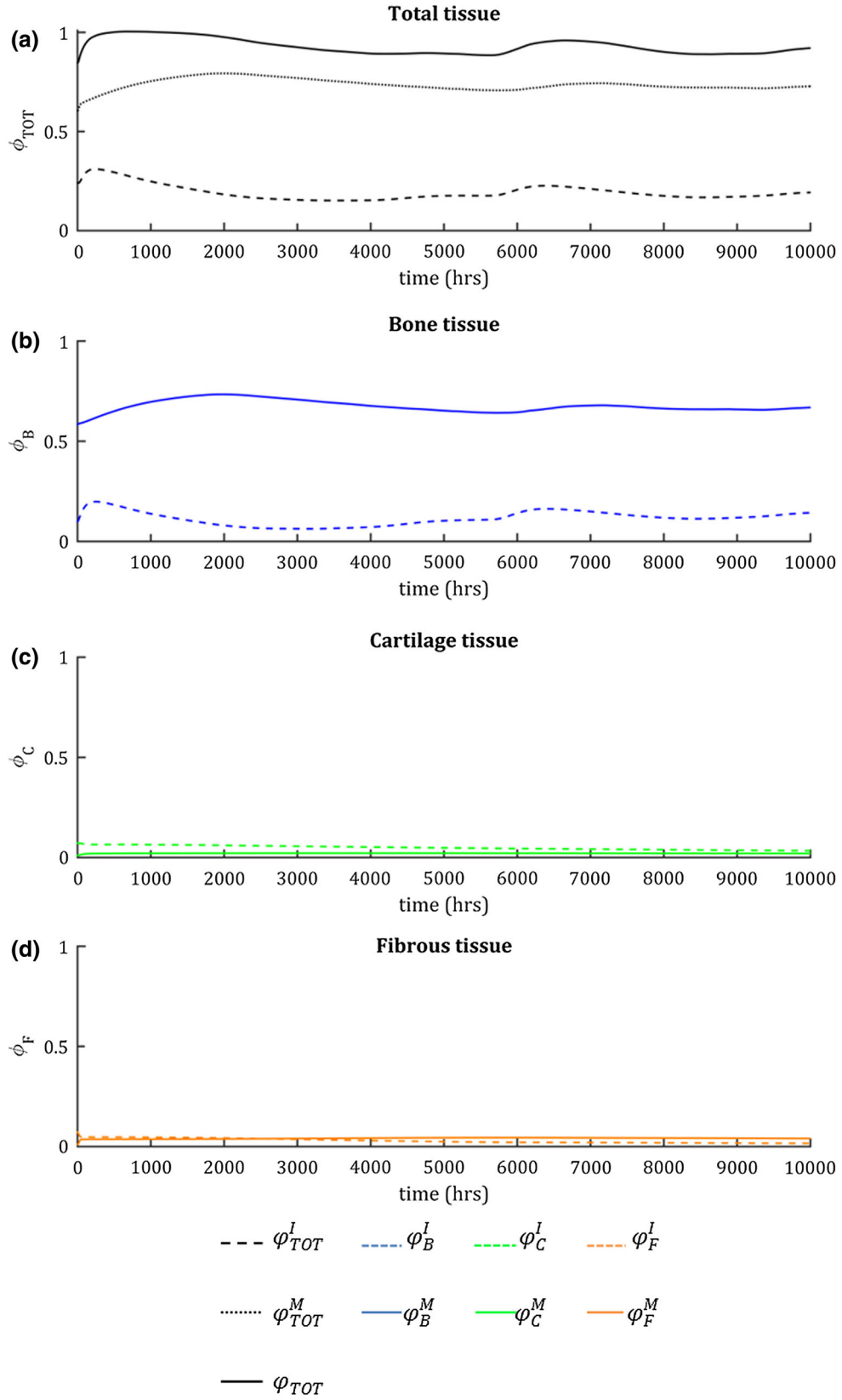
Fig. 8 The tissue volume fraction evolutions averaged across the entire beam for **a** total, **b** bone, **c** cartilage, and **d** fibrous tissue in *Simulation 1*
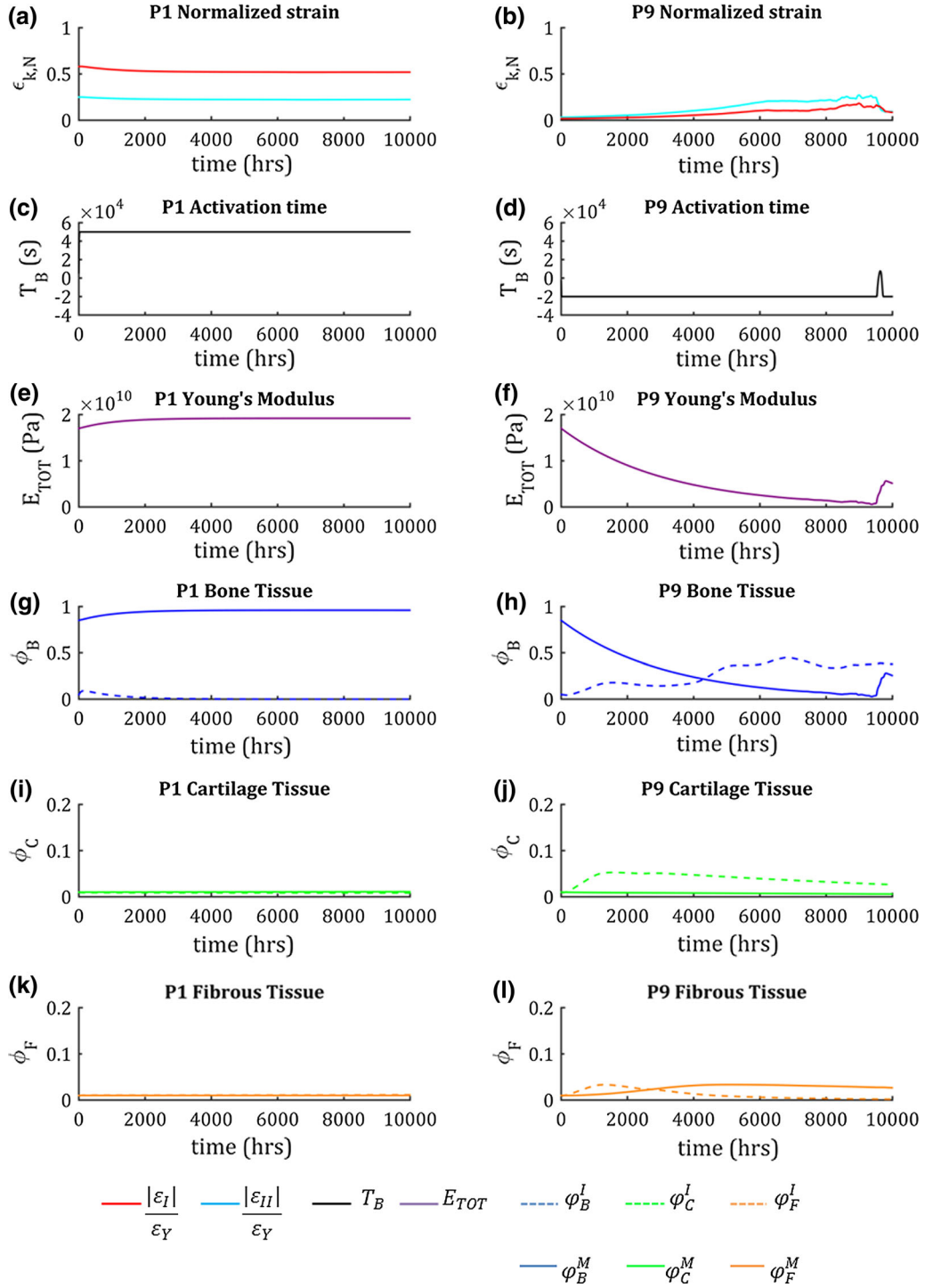
Fig. 9 Normalized principal strains, T_B, total Young's modulus, immature and mature tissue evolutions for each tissue type at points P1 and P6 in *Simulation 1*

bone tissue. The local Young's modulus at point P1 increases to its maximum permissible level (20 GPa) after approximately 3000 h as can be seen in Fig. 9e. The direct effect of this increase is to slightly reduce the level of strain in the tissue as the static loading remains constant.

Conversely, at point P9 the initial normalized strain is too low (<0.15) to drive T_B upwards and therefore T_B falls to the minimum value ($-20{,}000$ s) (Fig. 9d). As the simulation progresses the Young's modulus
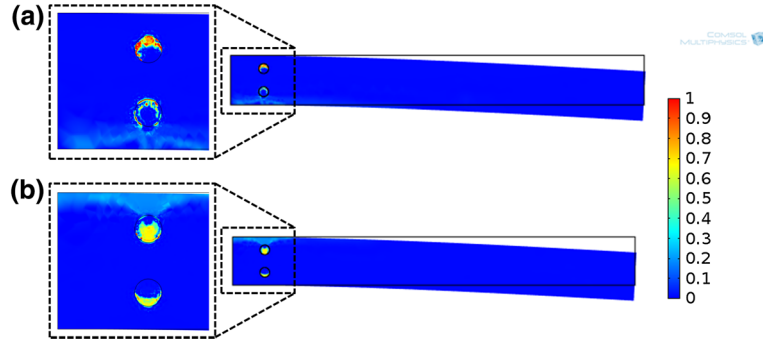
Fig. 10 The volume fraction of mature **a** cartilage and **b** fibrous tissues after 1000 h under static loading (2.5 MPa) (*Simulation 2*)
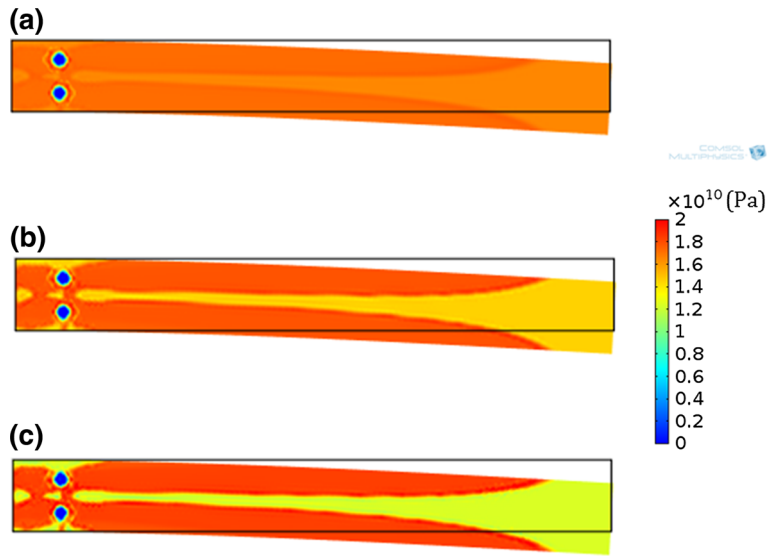
Fig. 11 The Young's modulus after **a** 100, **b** 500 and **c** 1000 h under static loading (2.5 MPa) (*Simulation 2*)

at point P9 steadily falls and the local strain around point P9 increases slowly until the activation time is increased above zero after approximately 90 h. This causes a localized increase in stiffness as the increase in T_B encourages the maturation of bone tissue (Fig. 9h). Significantly different patterns of tissue evolution can be observed between points P1 and P9. Point P1 corresponds to a cortical bone region of the mid-diaphysis where the entire volume is filled with mature bone tissue and therefore there is no free space for cells to diffuse or new tissue to grow in this region. However, at point P9 after the initial resorption of mature bone, due to the lower strains in this region, there is free space for cells to diffuse into. This effect can be seen as the levels of immature tissues increase at point P9 during the initial 1000 h of the simulation. Point P9 may be considered to be a cancellous bone region where there is a localized bone growth and remodeling which occurs toward the end of the simulation. This can be seen in *Videos 1* and 2.

Simulation 2 looked at a specimen with two voids perforating initially predominantly mature bone. Around and within the voids, cartilage and fibrous tissue formation dominated because of the particular local strain conditions, as can be seen in Fig. 10a. Along the upper surface the first principal strain is significantly higher than the second principal strain, nevertheless the second principal strain is large enough to locally initiate cartilage growth around the upper void. By the end of the simulation, φ_C^M has increased from almost zero to be the dominant tissue locally at the upper void. Similarly, in Fig. 10b, it can be seen that fibrous tissue has formed around the lower void.

Figure 11 shows the evolution of Young's modulus in *Simulation 2*. There is noticeable resorption around the upper and lower surfaces and around the voids near the fixed end. The normalized strain in these locations has been excessively high (> 1.8) for any new tissue to form and resorption has dominated. It is apparent that if

Table 1 Initial volume fractions and applied loads for each simulation

Simulation	Loading type		Initial volume fractions							Applied load (MPa)
	Static	Cyclic	φ_B^I	φ_B^M	φ_C^I	φ_C^M	φ_F^I	φ_F^M	φ_V	
1	x		0.05	0.85	0.01	0.01	0.01	0.01	0.06	2.5
			0.2	0.05	0.2	0.01	0.2	0.01	0.33	
2	x		0.05	0.85	0.01	0.01	0.01	0.01	0.06	2.5
3		x	0.05	0.85	0.01	0.01	0.01	0.01	0.06	$\sin\left(\frac{\pi t}{36{,}000}\right)$
			0.2	0.05	0.2	0.01	0.2	0.01	0.33	
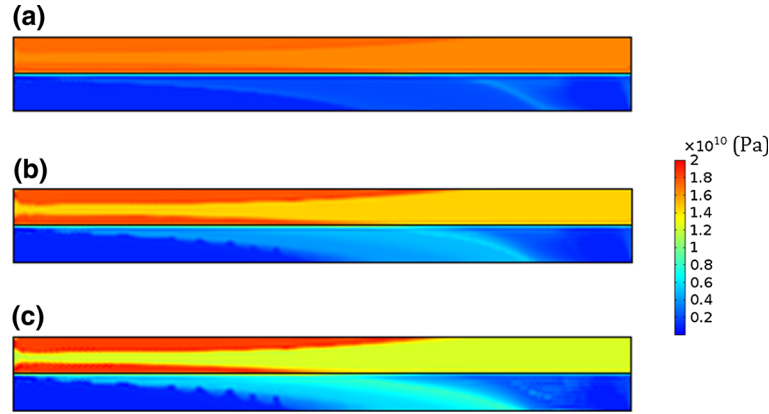
Fig. 12 The Young's modulus, E after **a** 100, **b** 500 and **c** 1000 h under cyclic loading (*Simulation 3*). The initial conditions were set for the upper half of the beam to be predominantly mature bone tissue and the lower half to be predominantly immature tissue
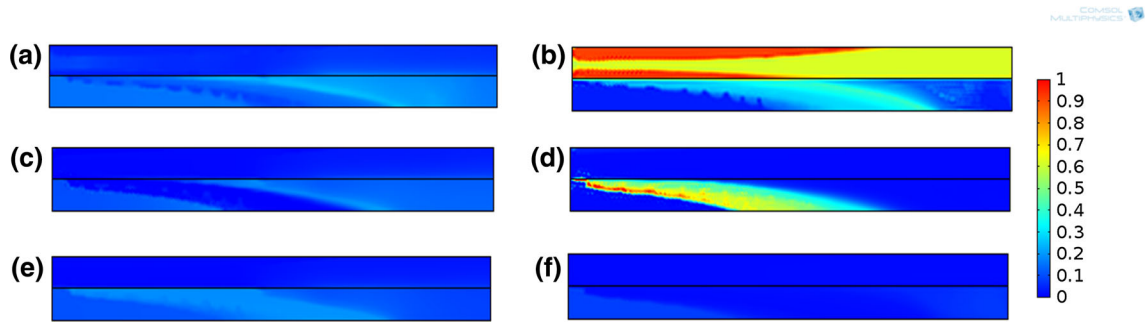
Fig. 13 The volume fractions of **a** immature bone, **b** mature bone, **c** immature cartilage, **d** mature cartilage, **e** immature fibrous and **f** mature fibrous after 1000 h from Simulation 3

the simulation were to continue for a longer period, the voids would effectively merge with the highly strained corner regions.

Simulation 3 investigated the scenario where the specimen was divided into two regions with different initial tissue volume fractions. The upper half of the beam was predominantly mature bone tissue (Table 1—row 4a), and the lower half was predominantly immature tissue (Table 1—row 4b). Cyclic loading was applied to this simulation ($P = \sin\left(\frac{\pi t}{36{,}000}\right) MPa$). It can be seen in Fig. 12 that after 1000 h there is a distinct region where the Young's modulus of the material has increased from initially < 1 to 8–10 GPa. This region corresponds to the section of the bone which has been strained to the levels required for tissue growth and maturation ($0.15 < \varepsilon_{I,N} < 0.85$ and $-0.15 < \varepsilon_{II,N} < -1.15$) and provides an insight into some degree of microstructural and macrostructural formation being locally adapted to the average strain distribution over time.

The tissue volume fractions after 1000 h of *Simulation 3* are shown in Fig. 13. Of particular interest is the region shown in Fig. 13b, d for the mature bone and cartilage tissues. There is a significant region of overlap

Table 2 Table of variables

Variable	Symbol	Value	Unit	References
Yield strain	ε_Y	0.006		[6]
Characteristic coefficients relating the change in $t_{\text{act},B}$ and $\varepsilon_{I,N}$	$a_{B,I}^{\varepsilon}\ b_{B,I}^{\varepsilon}\ c_{B,I}^{\varepsilon}$	$-6.25\ 6.25 - 0.5625$	s^{-1}	[4,9,20,32,33,64,71,92]
Characteristic coefficients relating the change in $t_{\text{act},B}$ and $\varepsilon_{II,N}$	$a_{B,II}^{\varepsilon}\ b_{B,II}^{\varepsilon}\ c_{B,II}^{\varepsilon}$	$-6.25\ 7.5 - 0.75$	s^{-1}	[4,9,20,32,33,64,71,92]
Characteristic coefficients relating the change in $t_{\text{act},C}$ and $\varepsilon_{II,N}$.	$a_C^{\varepsilon}\ b_C^{\varepsilon}\ c_C^{\varepsilon}$	$-12.5\ 25 - 11.5$	s^{-1}	[20,32]
Characteristic coefficients relating the change in $t_{\text{act},F}$ and $\varepsilon_{I,N}$	$a_F^{\varepsilon}\ b_F^{\varepsilon}\ c_F^{\varepsilon}$	$-5\ 12.5 - 6.8125$	s^{-1}	[20,32]
Bone growth rate coefficient	α_B	4E−5	m^2s^{-1}	[4,9,20,32,33,64,71,92]
Cartilage growth rate coefficient	α_C	1E−5	m^2s^{-1}	[20,32]
Fibrous growth rate coefficient	α_F	1E−5	m^2s^{-1}	[20,32]
Bone maturation rate coefficient	γ_B	2E−6	m^2s^{-1}	[1,4,64]
Cartilage maturation rate coefficient	γ_C	1E−5	m^2s^{-1}	
Fibrous maturation rate coefficient	γ_F	1E−3	m^2s^{-1}	
Mature bone resorption rate coefficient	β_B	1E−7	m^2s^{-1}	[28,62]
Mature cartilage resorption rate coefficient	β_C	1E−7	m^2s^{-1}	[28,62]
Mature fibrous resorption rate coefficient	β_F	1E−7	m^2s^{-1}	[28,62]
Diffusion coefficients for bone	$\lambda_B\ \Phi_B$	1E−10 1E−7	m^2s^{-1}	[82]
Diffusion coefficients for cartilage	$\lambda_C\ \Phi_C$	1E−10 1E−7	m^2s^{-1}	[82]
Diffusion coefficients for fibrous	$\lambda_F\ \Phi_F$	1E−10 1E−7	m^2s^{-1}	[82]
$\left(T_i^{Bound}\right)$ coefficients for bone, cartilage and fibrous	$p_i^{\text{Bound}}\ q_i^{\text{Bound}}\ r_i^{\text{Bound}}$	1 10,000 20,000	S	
$\left(T_i^{M}\right)$ coefficients for bone, cartilage and fibrous	$d_i^M\ e_i^M\ f_i^M$	1 30,000 10,000	S	
$\left(T_B^{R}\right)$ coefficients for bone	$k_B^R\ l_B^R\ m_B^R$	$1-15{,}000\ 10{,}000$	S	
$\left(T_C^{R}\right)$ coefficients for cartilage	$k_C^R\ l_C^R\ m_C^R$	$1-5000\ 10{,}000$	s	
$\left(T_F^{R}\right)$ coefficients for fibrous	$k_F^R\ l_F^R\ m_F^R$	$1-5000\ 10{,}000$	s	
Activation time growth threshold	$T_{B,GT}\ T_{C,GT}\ T_{F,GT}$	20,000 30,000 10,000		
Immature tissue Young's Modulus	$E_B^I\ E_C^I\ E_F^I$	1E7 1E6 1E6	Pa	[3,10,64,69]
Mature tissue Young's Modulus	$E_B^M\ E_C^M\ E_F^M$	20E9 1E8 1E6	Pa	[5,15,22,43,65,69]
Young's Modulus of free space	E_V	0	Pa	
Activation time range	$T_i^{\text{Min}}\ T_i^{\text{Max}}$	$-20000\ 50{,}000$	s	

between these two tissues indicating that, as the simulation progresses, the cartilage tissue is maturing and then being resorbed and converted into calcified mature bone tissue.

4 Discussion

The work presented here has added to the previous model of bone formation from Schmitt and colleagues [82] a strain dependence on tissue growth and the inclusion of a strain-dependent maturation time for each tissue by introducing multi-tissue evolution (bone, cartilage and fibrous). Included in this new model is a

distinction between the types of tissues which will be formed during not only osteogenesis but tissue evolution in general. This is of particular interest for modeling the behavior of bone formation around implant and prosthetic devices [47,54,71], fracture healing and bone remodeling. The model proposed here provides a framework for integrating the distinct processes of bone remodeling, fracture healing and osseointegration under one numerical model. Unlike similar models [24,35,41,61] the process of bone remodeling and fracture healing are controlled by the same mechanical stimuli to determine tissue volume fractions, rather than cell concentrations and ECM development directly. There is no independent bone remodeling formulation used, but rather all tissue evolution is deemed to follow the same mechano-biological pathways for remodeling. This approach allows for greater flexibility in the model and a reduced number of input parameters. Three simulations were carried out to identify the homeostasis of the model and to test localized tissue evolutions.

The results from *Simulation 1* showed that a steady state was reached in terms of bone tissue volume fractions, both globally and locally. *Simulation 1* also revealed that the majority of bone growth occurred early in the simulation (the first 500 h) and that the remodeling was dependent and adaptive to the local strain environment. Two distinct bone regions formed during *Simulation 1* which resemble the cortical and cancellous architecture observed in long bones. The Young's modulus was observed to reach a maximum value of 20 GPa in the cortical-like region and stabilized between 7 and 11 GPa in the cancellous-like region (Fig. 7, *Video 1*). This is consistent with the reported values of modulus for cortical and cancellous bone [6,76]. The resorption rate observed in under strained regions is corroborated by those observed in astronauts and bed-rest studies where a drop in bone density of around 20% has been measured in a 4–6-week period [28,62].

In *Simulation 2* there were noticeable formations of cartilage and fibrous tissue in and around the voids. This finding could reveal a link to the fibrous tissue formations observed around implants [54] where a similar bone-implant gap may provide a strain environment conducive to fibrous tissue formations. Predicting the formation of inferior interface tissue would be of significant value for the development of future prosthetic devices [90]. The model does not pretend to capture interfacial effects which are known to be central to the integration of implants and in particular to the fibrosis. These effects depend mostly on the physical-chemistry of implant surfaces and involve very specific biological processes that are not implemented here in the mechano-biological description. Alternatively, the proposed model provides a way to determine the contribution of mechanical effects to osseointegration or bone fracture healing, in situations where several tissues might be involved. Moreover, the ability of this model to differentiate between tissue types allows significant flexibility for the prediction of tissue growth and adaptation to changes in the local material properties [57,66,71,83].

Similarly, *Simulation 3* predicted locally specific tissue formations with distinguishable geometric features being generated and driven by the regional strain distribution. This effect may be indicative of the global bone geometry being optimized to the loading conditions. Additionally, the simulated formation of interspersed mature cartilage and bone tissues in the lower half of the beam is congruent with the findings of Salisbury et al. [79] where an artificial cyclic loading was applied to damaged canine tibias in vivo and an increase in the formation of cartilage tissue was observed when compared to the control. The rate of bone healing also increased as the cartilaginous tissue calcified more rapidly than bone formed in the control experiments. Cartilage tissue was found to be interspersed among the bone tissue around the damaged region after 38 days (900 h) [79]. This corroborates the findings in our study where, in *Simulation 3* (Fig. 13b, d), mature cartilage and bone tissue are seen to form in the same region of the lower half of the beam after 1000 h (40 days). Figure 14 shows a comparison between the volume fractions of mature cartilage and mature bone tissues from *Simulation 3* and the results from Salisbury-Palomares et al. [79]. It can be seen that *Simulation 3* predicts a volume fraction of mature cartilage which matches closely with the experimental results after 38 days. *Simulation 3* also predicts a volume fraction of mature bone tissue slightly lower than that of the experimental results after 38 days. Differences between the two tissue evolution trends may be attributable to the parameterization of the model, model geometry and differences in the initial tissue volume fractions. Furthermore, the cross over area where both bone and cartilage form is of particular interest because as the cartilage matures it introduces a stiffening effect to the tissue (when compared solely to the immature tissue). Such stiffening will reduce the strain locally and subsequently initiate the formation of bone tissue in the same region [81].

The variable $t_{\text{act},i}$ was used to quantify the accumulation of strain over time for each tissue, where the change in $t_{\text{act},i}$ was controlled by the local strain in the material. The rationale for this description was to account for microcracking, microdamage and fatigue as time progresses, rather than an instantaneous phenomenon [4,12,43,50,64,74,95]. More generally, this work proposes that the accumulation of tissue specific microdamage over time is a driving factor in remodeling. This accumulation can be monitored by compounding the previous strain levels experienced in the material. Consequently, this introduces a time dependence on the remodeling
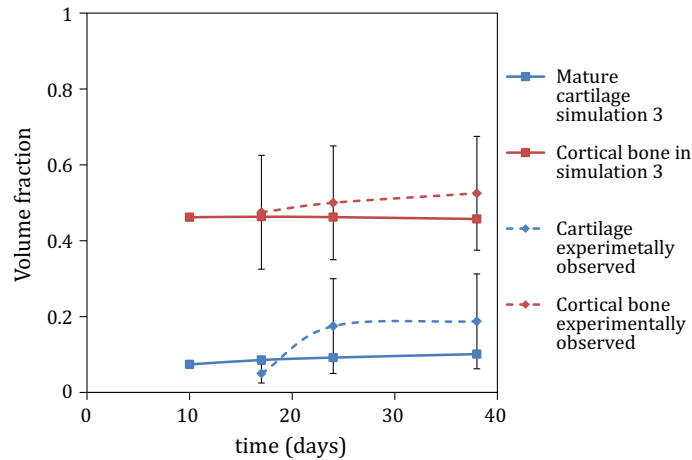
Fig. 14 A comparison between the volume fractions of mature cartilage and bone from *Simulation 3* and those experimentally observed by [79]; the error bars represent the standard deviation in experimental results

process where strain must be maintained and repeatedly reinitiated for remodeling to begin and propagate [1,4,64].

The principal strains have been used as the mechanical characteristic for defining the diffusion, growth, resorption and maturation of each tissue. Recent studies have investigated the importance of normal strains, shear strain, hydrostatic strains and fluid flows on the adaptation of bone [91]. The formation of bone both on and away from the neutral axis during in vivo bending of murine tibias has indicated that the effects of shear may be an important factor in bone adaptation [87]. In addition to shear strains in the material, the surface shear fluid flow produced from a hydrostatic pressure may be considered another important contributor for osteogenesis [85,86]. Fluid shear was not considered in this work, but there is potential to include this through a poro-elastic material model. The deviatoric strain, which removes the effects of the hydrostatic strain and only considers the geometrical distortions, would be an effective method for comparing tissues with significantly different material properties because this would enable a more direct comparison between materials with radically different porosities, stiffness and fluid fractions [47,48].

This is of particular significance when considering the differentiation of MSCs around grafts or scaffolds [14,20,57,71] and typically the magnitude of strain observed during cell differentiation (5–15%) is an order of magnitude higher than those observed in the normal physiological range (< 1%) of cortical bone [20,45,71,75]. The difference in stiffness between a region of formed bone around a fracture site and a scaffold site filled with fibrous tissues and undifferentiated MSCs would produce locally high strains within the scaffold voids, whereas the rigid bone would limit strains to those experienced physiologically. In the model presented here, the immature tissue volume fractions are considered to be descriptive of tissue formations a couple of days after the colonization of MSC in a region where immature tissue has already begun to form.

An isotropic linear elastic material model was used for all tissue types in this study primarily because of the reduced complexity required in the numerical simulations [91]. Including more complex material models for each tissue would aid in providing more accurate tissue-specific predictions, specifically in circumstances where material behavior is of a greater significance in the overall material response. For bone tissue, the model may be developed by including the influence of poro-elastic, viscoelastic and anisotropic material behaviors [37,37,37,40]. This would allow porosity, strain rate and tissue heterogeneity to be added as determining factors in tissue remodeling [43,45,96] which is of particular importance in defining the yield strain and Young's modulus for cortical bone. A linear elastic material model for describing cartilage tissue has been used in previous studies [5,34] and is believed to be sufficiently descriptive of the tissue behavior [15]. Considering other soft tissue material behaviors such as hyperelasticity, anisotropy and viscoelasticity would provide a more realistic description of both cartilage and fibrous tissues [30]. Similarly using a higher value for the Poisson's ratio for cartilage in the region of 0.49 would provide a more accurate description of the high fluid content and incompressibility of cartilage. Fibrous tissue has been considered in this model to generally consist of connective tissues with a significantly lower stiffness than both bone and cartilage. To fully describe fibrous

tissue, a more complete description would be required in order to account for the non-linear hyperelastic material behavior observed in fibrous tissues around implants [30,54]. Tissue-specific material models are required to provide a more realistic description of bone, cartilage and fibrous tissues and to help draw the distinction between the immature and mature tissue phases. Similarly, the anisotropy of cortical and trabecular bone is well documented, the particular material properties of these specific types of bone material may provide a more accurate modeling prediction. It is also worth noting, however, that a certain degree of material anisotropy has been predicted in all three simulations presented here, where an initially uniform Young's modulus distribution has been transformed into a non-uniform material property distribution. This finding may have the potential to provide insight into the adaption of the structure of bone, at various length scales, to the mechanical environment. This would explain the emergence of anisotropy in mature bone material, at the macro- and microstructural levels, as being driven and controlled by the external loading environment and the localized internal strains. However, it may also be appropriate to consider the remodeling as being controlled by the anisotropy inherent in the material itself ([26]). In addition to this, including the influence of porosity, void spaces and material heterogeneity, as was used in *Simulations 2 and 3*, may also provide an insight into the adaptability of bone's microstructure to the loading environment. The volume fraction of free space φ_V accounts for this to a certain extent; however, it does not explicitly describe the interaction between the microstructural void spaces and new tissue formation. In this study, it has been assumed that a complete volume fraction of mature bone tissue represents fully formed cortical bone with a normal porosity in the material of between 5 and 10% [8,63,75].

Future work will include experimental validation of the presented model. This will certainly require the many parameters used in the model to be adequately and realistically tuned to fit with specific animal models. This may focus on histological studies of tissue around implants and attempt to corroborate the observed tissue formations with equivalent simulation predictions. By recreating different tissue distributions observed under unique loading conditions, a greater degree of confidence in the model's predictions will be gained. Similarly, the replication of structural and microstructural geometries observed in trabecular, cortical and macroscale bone may be achievable through recreations of the loading conditions known to enact upon the skeleton. Such a recreation would interlink musculoskeletal forces with geometrically observed bone structures. Furthermore, the homeostasis observed in *Simulation 1* may be investigated further by determining the volume fraction of mature bone content reached at a particular steady state and how this is related to the applied loading. Such a relationship between loading conditions and steady-state mechanical properties [60] may be significant in predicting bone structures, such as cortical thickness or cross-sectional second moment of area, in long bones.

5 Conclusion

This work reports a numerical description of tissue evolution accounting for the presence and mechanical interactions between several tissue types, namely bone, cartilage and fibrous tissues. It was built upon a previous model of osteogenesis [82] by including several new mechano-biological criteria, such as a distinction between several tissue types, a strain dependence on tissue growth, and strain controlled tissue maturation. For a series of simple specimen geometries, tissue evolution in accordance with the local mechanical environment has been demonstrated and has showed to reach a homeostasis. Furthermore, specific tissue formations driven by local strain distributions have been demonstrated around void spaces at different locations in the specimen. Likewise, the generation of cartilage tissue interspersed with bone tissue, similar to that observed during the fracture healing process, has been recreated at realistic tissue formation rates. Being able to predict tissue evolution is of importance in several biological processes, in particular around an implant, during fracture healing and during bone remodeling. This is especially significant in the circumstances where there is fibrous tissue formation causing poor mechanical integration with the surrounding bone and subsequent mechanical loosening of implants. While the model was applied here to osteoarticular tissues, the proposed formulation could be applied to other tissue types, in cardiovascular tissues for instance. Accurately understanding the formation process of new tissues and the loading conditions required to produce stable integration may prove to be a powerful tool in improving implant success rates.

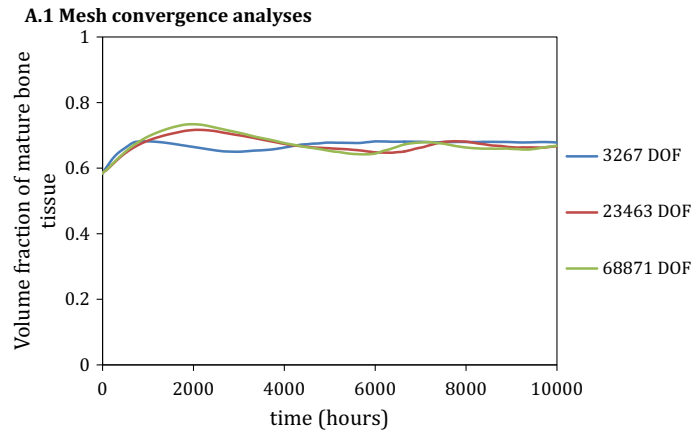## A.1 Mesh convergence analyses

A.1 Mesh convergence analyses

Fig. 15 Mesh convergence for *Simulation 1*. Coarse mesh (blue) (3267 DOF), refined mesh (red) (23463 DOF) and extra refined mesh (green) (68871 DOF). The mesh was refined globally between each refinement
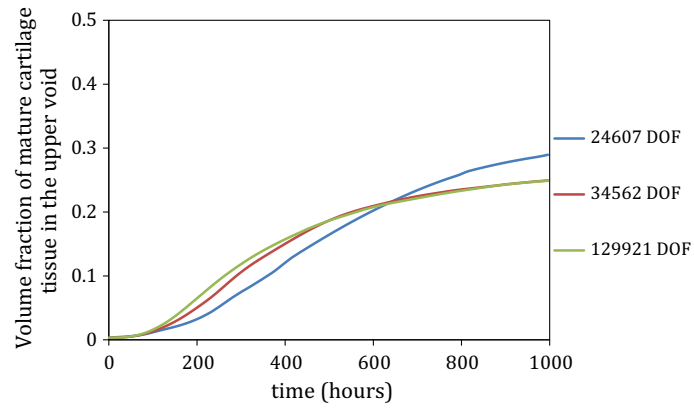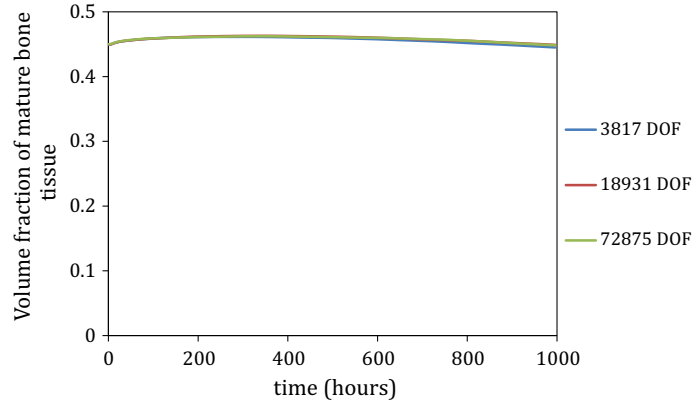

Fig. 16 Mesh convergence for *Simulation 2*. Coarse mesh (blue) (24607 DOF), refined mesh (red) (34562 DOF) and extra refined mesh (green) (129921 DOF). The mesh was refined locally around both voids between each refinement

Fig. 17 Mesh convergence for *Simulation 3*. Coarse mesh (blue) (3817 DOF), refined mesh (red) (18931 DOF) and extra refined mesh (green) (72875 DOF). The mesh was refined globally between each refinement

A.2 Detailed results for *Simulation 1*
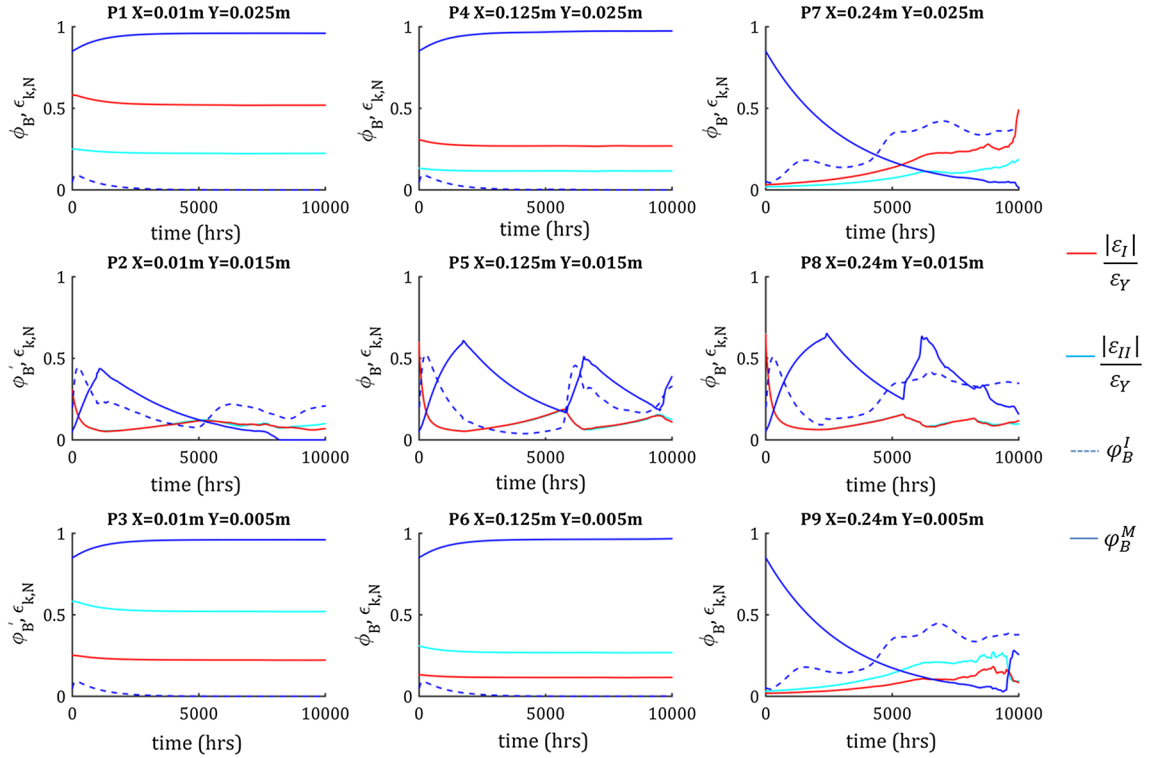
Fig. 18 Bone tissue evolution during static loading (*Simulation 1*)
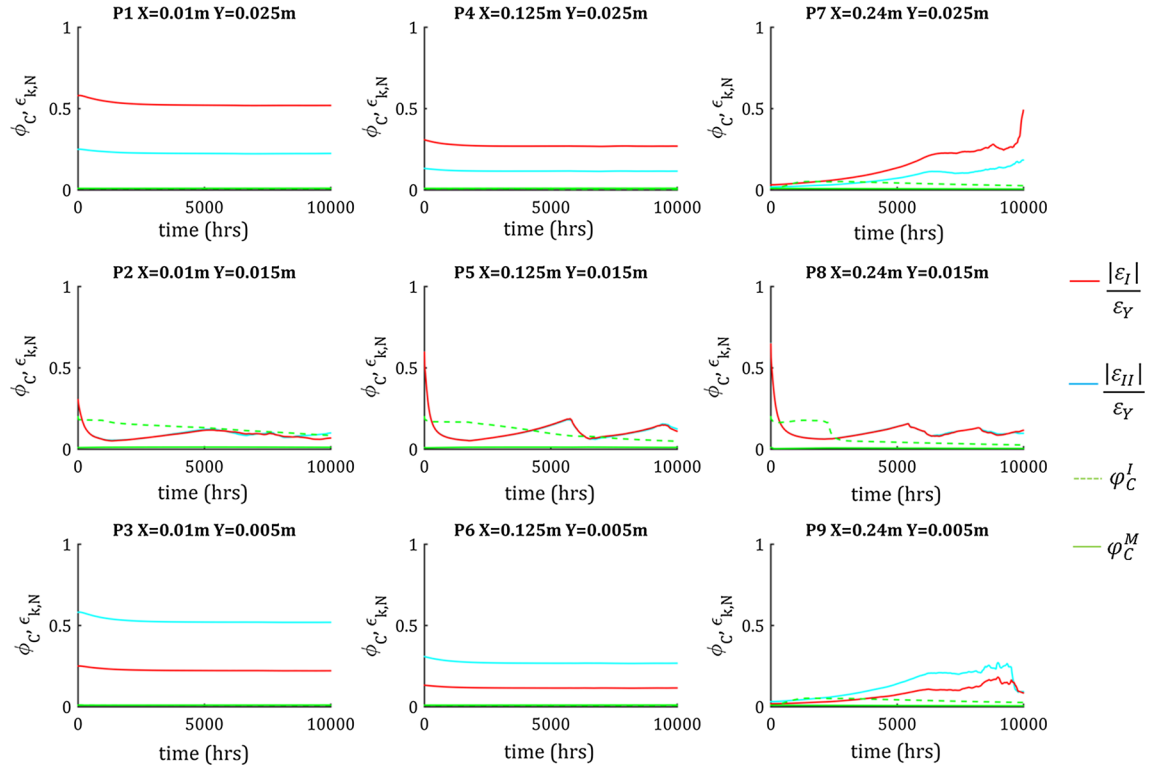
Fig. 19 Cartilage tissue evolution during static loading (*Simulation 1*)
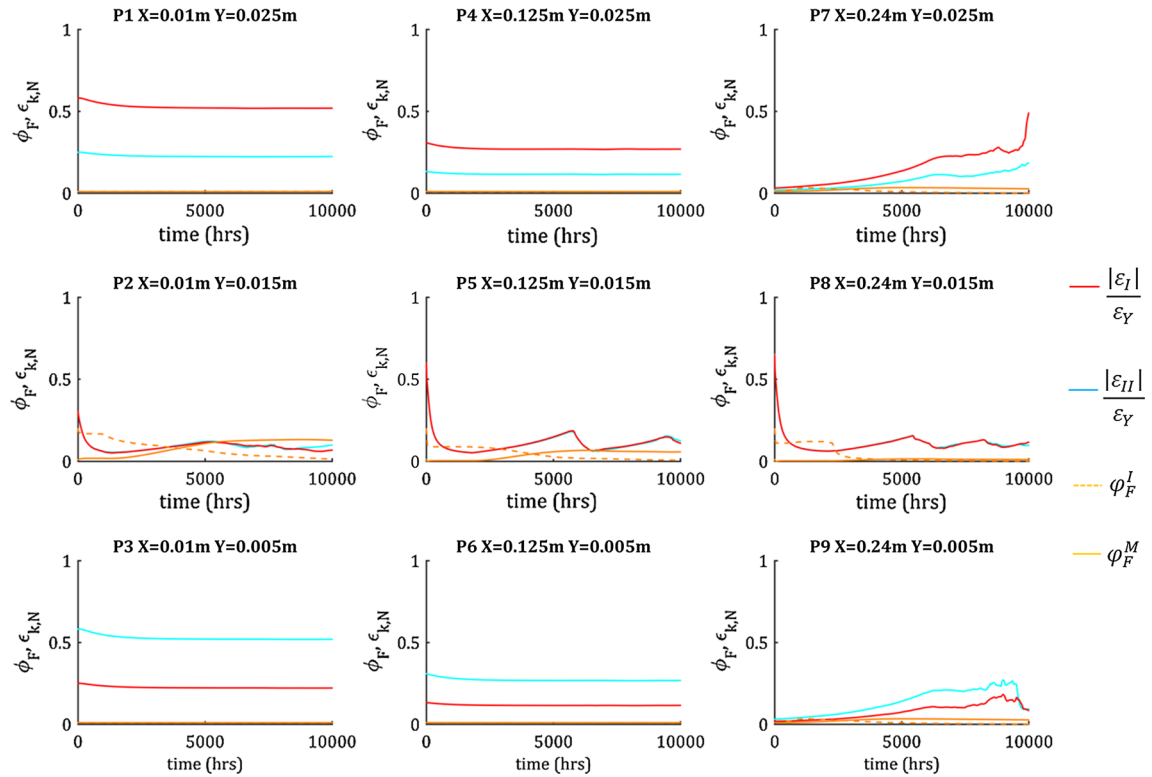
Fig. 20 Fibrous tissue evolution during static loading (Simulation 1)

A.3 Detailed results for *Simulation 2*
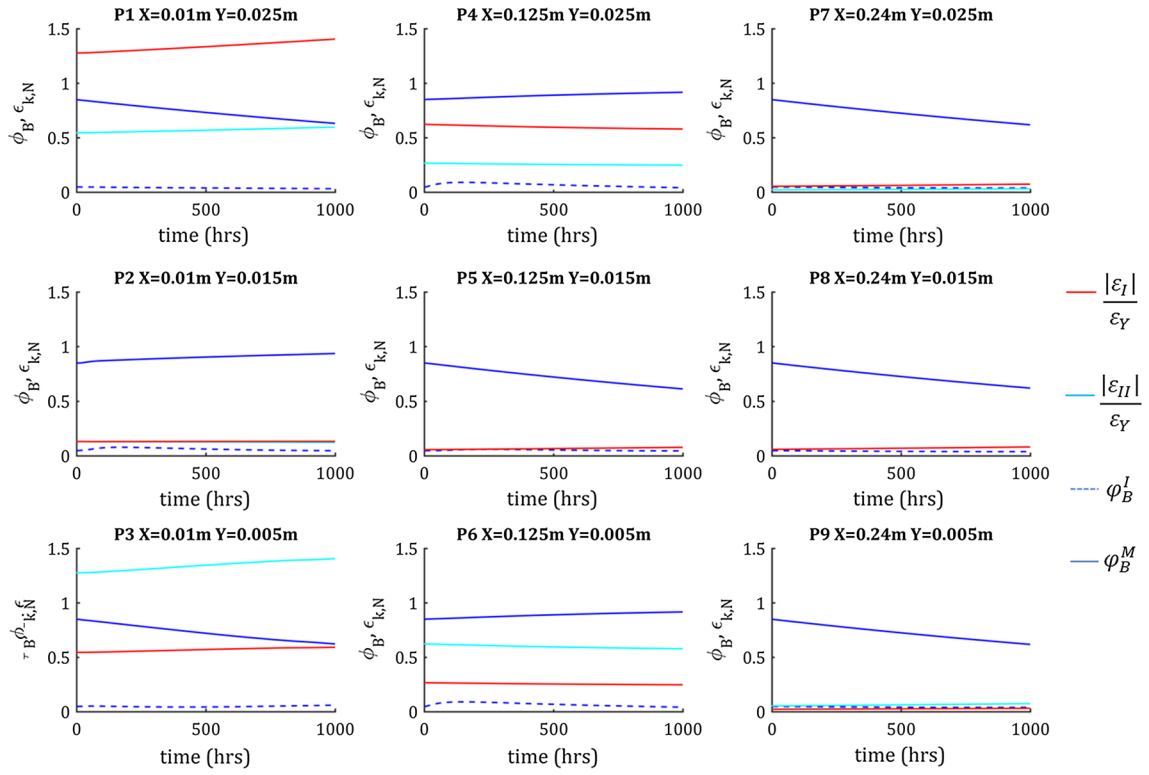
Fig. 21 Bone tissue evolution, heterogeneous initial conditions with voids and static loading (*Simulation 2*)
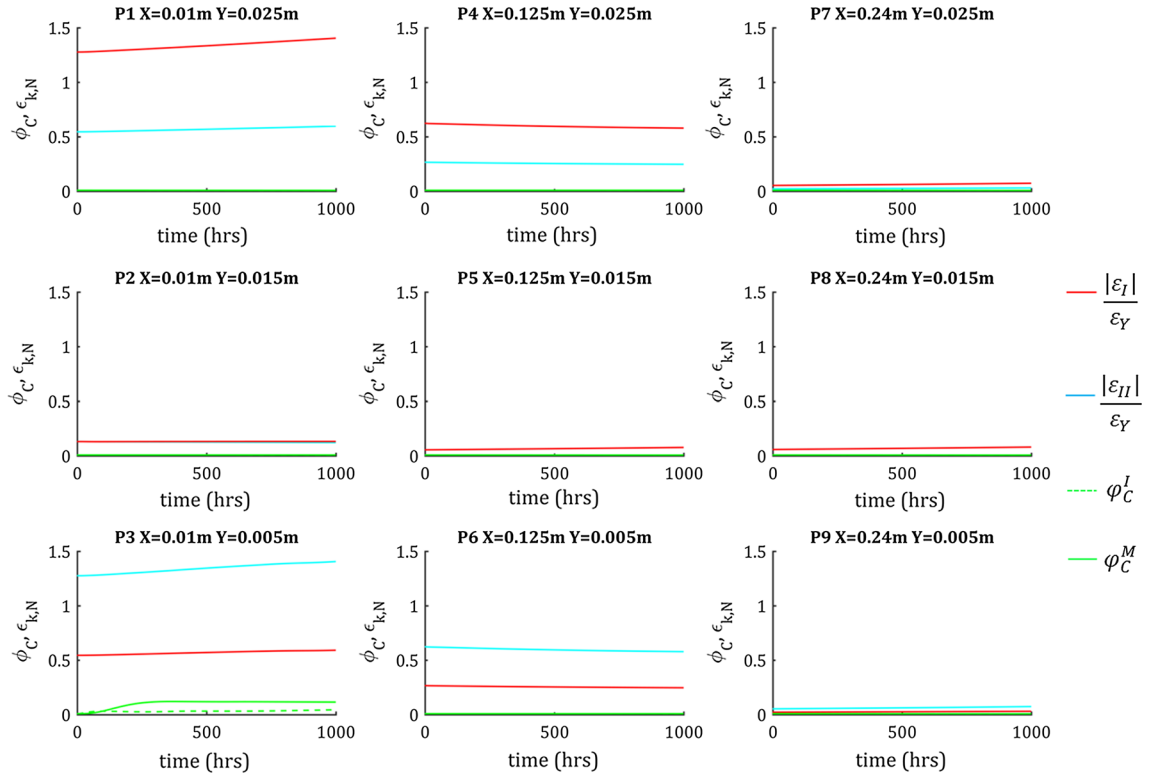
Fig. 22 Cartilage tissue evolution, heterogeneous initial conditions with voids and static loading (*Simulation 2*)
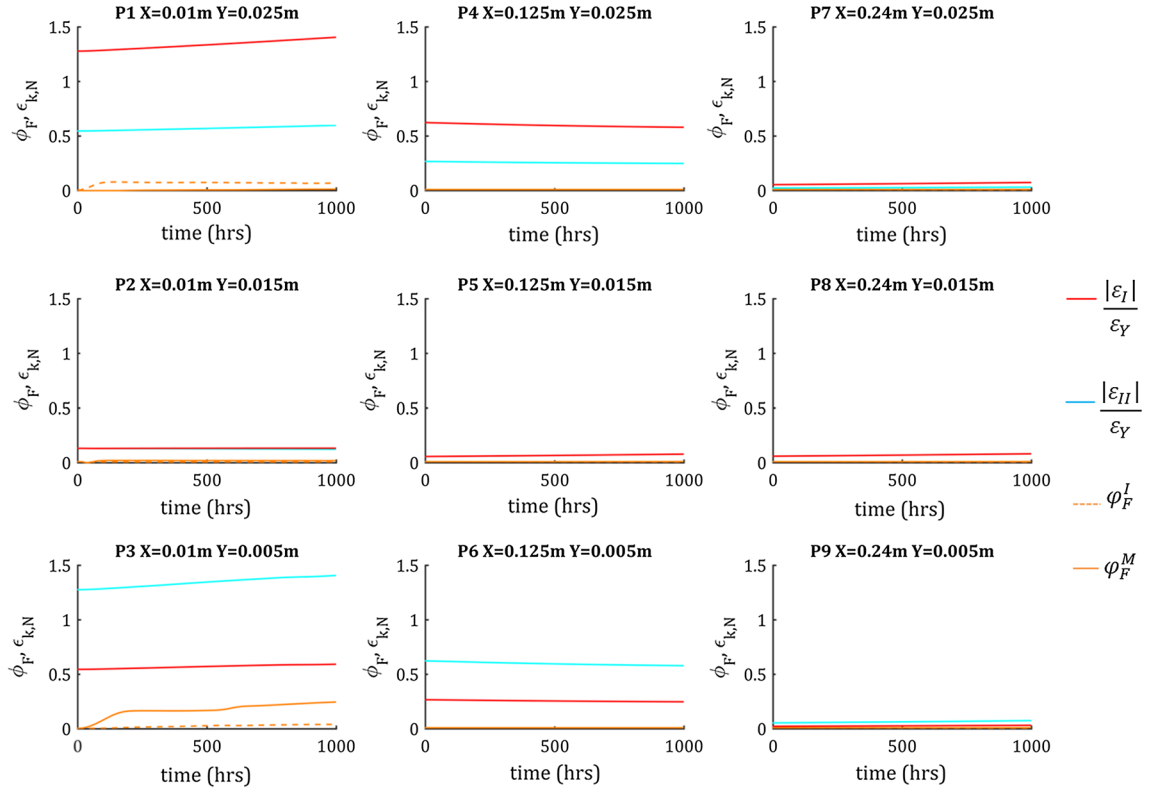
Fig. 23 Fibrous tissue evolution, heterogeneous initial conditions with voids and static loading (*Simulation 2*)

A.4 Detailed results for *Simulation 3*
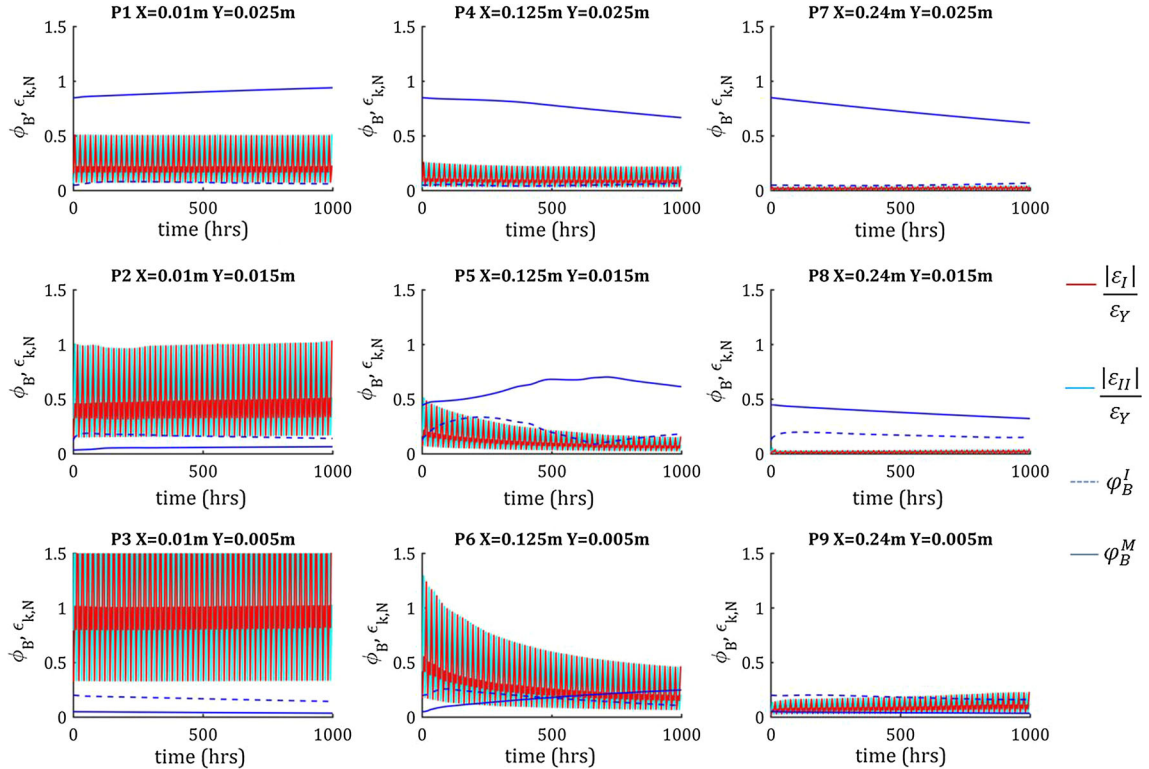
Fig. 24 Bone tissue evolution, heterogeneous initial tissue volume fractions and cyclic loading (*Simulation 3*)
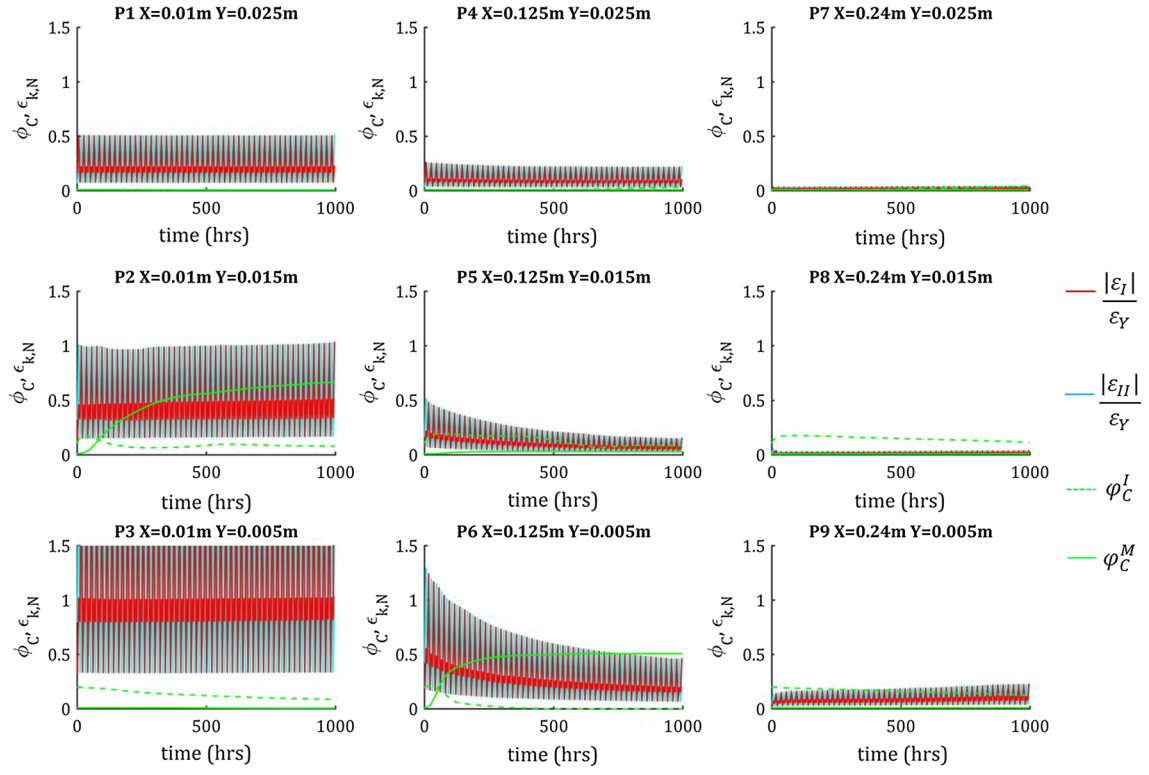
Fig. 25 Cartilage tissue evolution, heterogeneous initial tissue volume fractions and cyclic loading (*Simulation 3*)
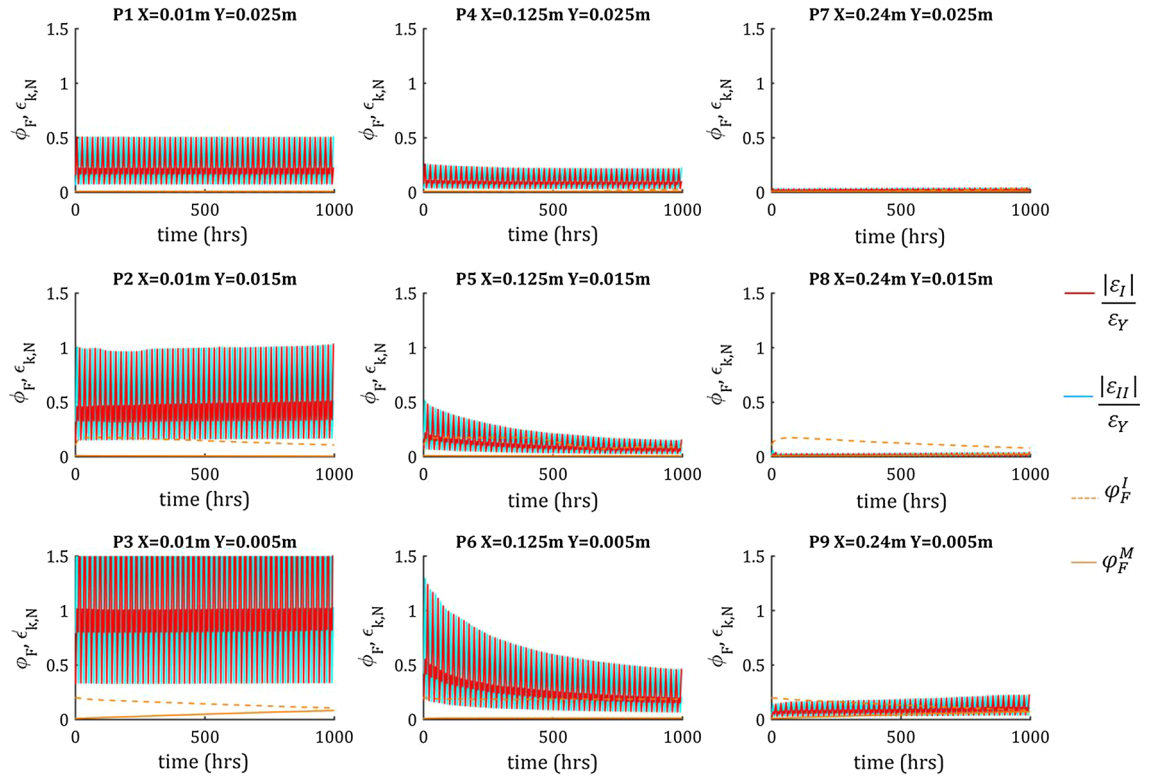

Fig. 26 Fibrous tissue evolution, heterogeneous initial tissue volume fractions and cyclic loading (*Simulation 3*)

References

1. Akkus, O., Polyakova-Akkus, A., Adar, F., Schaffler, M.B.: Aging of microstructural compartments in human compact bone. J Bone Miner. Res. **18**(6), 1012–1019 (2003). https://doi.org/10.1359/jbmr.2003.18.6.1012
2. Avval, P.T., Bougherara, H.: Predicting bone remodeling in response to total hip arthroplasty?: Computational study using mechanobiochemical model. J. Biomech. Eng. **136**(5), 1–12 (2017). https://doi.org/10.1115/1.4026642
3. Bala, Y., Depalle, B., Douillard, T., Meille, S., Clément, P., Follet, H., Boivin, G.: Respective roles of organic and mineral components of human cortical bone matrix in micromechanical behavior: an instrumented indentation study. J. Mech. Behav. Biomed. Mater. **4**(7), 1473–82 (2011). https://doi.org/10.1016/j.jmbbm.2011.05.017
4. Bala, Y., Farlay, D., Delmas, P.D., Meunier, P.J., Boivin, G.: Time sequence of secondary mineralization and microhardness in cortical and cancellous bone from ewes. Bone **46**(4), 1204–1212 (2010). https://doi.org/10.1016/j.bone.2009.11.032
5. Bandeiras, C., Completo, A.: A mathematical model of tissue-engineered cartilage development under cyclic compressive loading. Biomech. Model. Mechanobiol. **16**(2), 1–16 (2016). https://doi.org/10.1007/s10237-016-0843-9
6. Bayraktar, H.H., Morgan, E.F., Niebur, G.L., Morris, G.E., Wong, E.K., Keaveny, T.M.: Comparison of the elastic and yield properties of human femoral trabecular and cortical bone tissue **37**, 27–35 (2004). https://doi.org/10.1016/S0021-9290(03)00257-4
7. Beaupré, G.S., Orr, T.E., Carter, D.R.: An approach for time-dependent bone modeling and remodeling—application: a preliminary remodeling simulation. J. Orthop. Res. **8**(5), 662–670 (1990)
8. Bousson, V., Meunier, A., Bergot, C., Vicaut, E., Rocha, M.A., Morais, M.H., Laredo, J.D.: Distribution of intracortical porosity in human midfemoral cortex by age and gender. J. Bone Miner. Res. **16**(7), 1308–1317 (2001). https://doi.org/10.1359/jbmr.2001.16.7.1308
9. Burr, D.B., Martin, R.B.: Errors in bone remodeling: toward a unified theory of metabolic bone disease. Am. J. Anat. **186**(2), 186–216 (1989). https://doi.org/10.1002/aja.1001860208
10. Burstein, A. H., Zika, J. M., Heiple, K. G., & Klein, L.: (1975) Contribution of collagen and mineral to the elastic-plastic properties of bone. *Journal of JBone and Joint Surgery*
11. Byrne, D.P., Lacroix, D., Prendergast, P.J.: Simulation of fracture healing in the tibia: Mechanoregulation of cell activity using a lattice modeling approach. J. Orthop. Res. **29**(10), 1496–1503 (2011). https://doi.org/10.1002/jor.21362
12. Cardoso, L., Herman, B.C., Verborgt, O., Laudier, D., Majeska, R.J., Schaffler, M.B.: Osteocyte apoptosis controls activation of intracortical resorption in response to bone fatigue. J. Bone Miner. Res. **24**(4), 597–605 (2009). https://doi.org/10.1359/jbmr.081210
13. Carter, D.R., Beaupré, G.S., Giori, N.J., Helms, J.A.: Mechanobiology of skeletal regeneration. Clin. Orthop. Relat. Res. **355**, 41–55 (1998)
14. Carter, D.R., Blenman, P.R., Beaupre, G.S.: Correlations between mechanical-stress history and tissue differentiation in initial fracture-healing. J. Orthop. Res. **6**(5), 736–748 (1988)
15. Carter, D.R., Wong, M.: Modelling cartilage mechanobiology. Philos. Trans. R. Soc. Lond. B Biol. Sci. **358**(1437), 1461–1471 (2003). https://doi.org/10.1098/rstb.2003.1346
16. Checa, S., Prendergast, P.J., Duda, G.N.: Inter-species investigation of the mechano-regulation of bone healing: comparison of secondary bone healing in sheep and rat. J. Biomech. **44**(7), 1237–1245 (2011). https://doi.org/10.1016/j.jbiomech.2011.02.074
17. Chen, J., Rungsiyakull, C., Li, W., Chen, Y., Swain, M., Li, Q.: Multiscale design of surface morphological gradient for osseointegration. J. Mech. Behav. Biomed. Mater. **20**, 387–397 (2013). https://doi.org/10.1016/j.jmbbm.2012.08.019
18. Christen, P., Ito, K., Ellouz, R., Boutroy, S., Sornay-Rendu, E., Chapurlat, R.D., van Rietbergen, B.: Bone remodelling in humans is load-driven but not lazy. Nat. Commun. **5**, 4855 (2014). https://doi.org/10.1038/ncomms5855
19. Claes, L., Augat, P., Suger, G., Wilke, H.J.: Influence of size and stability of the osteotomy gap on the success of fracture healing. J. Orthop. Res. **15**(4), 577–584 (1997). https://doi.org/10.1002/jor.1100150414
20. Claes, L., Heigele, C.A.: Magnitudes of local stress and strain along bony surfaces predict the course and type of fracture healing. J. Biomech. **32**(3), 255–266 (1999). https://doi.org/10.1016/S0021-9290(98)00153-5
21. Currey, J.D.: The Mechanical Adaptations of Bones. Princeton University Press, Princeton (1984)
22. Currey, J.D.: The effect of porosity and mineral content on the Young's modulus of elasticity of compact bone. J. Biomech. **21**(2), 131–139 (1988). https://doi.org/10.1016/0021-9290(88)90006-1
23. Dabirrahmani, D., Hogg, M., Kohan, L., Gillies, M.: Primary and long-term stability of a short-stem hip implant. In: Proceedings of the Institution of Mechanical Engineers, vol. 224 no 9, (2010)
24. Doblaré, M., García-Aznar, J.M.: On numerical modelling of growth, differentiation and damage in structural living tissues. Arch. Comput. Methods Eng. **13**(4), 471–513 (2006). https://doi.org/10.1007/BF02905856
25. Doblaré, M., García, J.M.: Application of an anisotropic bone-remodelling model based on a damage-repair theory to the analysis of the proximal femur before and after total hip replacement. J. Biomech. **34**(9), 1157–1170 (2001). https://doi.org/10.1016/S0021-9290(01)00069-0
26. Doblaré, M., García, J.M.: Anisotropic bone remodelling model based on a continuum damage-repair theory. J. Biomech. **35**(1), 1–17 (2002). https://doi.org/10.1016/S0021-9290(01)00178-6
27. Doblaré, M., Garcia, J.M., Gomez, M.J.: Modelling bone tissue fracture and healing: a review. Eng. Fract. Mech. **71**(13–14), 1809–1840 (2004). https://doi.org/10.1016/j.engfracmech.2003.08.003
28. Donaldson, C.L., Hulley, S.B., Vogel, J.M., Hattner, R.S., Bayers, J.H., Mcmillan, D.E.: Effect of prolonged bed rest on bone mineral. Metabolism **19**(12), 1071–1084 (1970). https://doi.org/10.1016/0026-0495(70)90032-6
29. Edwards, J., Schulze, E., Sabokbar, A., Gordon-Andrews, H., Jackson, D., Athanasou, N.A.: Absence of lymphatics at the bone-implant interface—implications for periprosthetic osteolysis. Acta Orthop. **79**(2), 289–294 (2008). https://doi.org/10.1080/17453670710015175
30. Freutel, M., Schmidt, H., Durselen, L., Ignatius, A., Galbusera, F.: Finite element modeling of soft tissues: material models, tissue interaction and challenges. Clin. Biomech. **29**(4), 363–372 (2014). https://doi.org/10.1016/j.clinbiomech.2014.01.006
31. Frost, H.M.: The Physiology of Cartilaginous Fibrous, and Bony Tissue. Charles C Thomas, Springfield (1972)

32. Frost, H.M.: Vital biomechanics: proposed general concepts for skeletal adaptations to mechanical usage. Calcif. Tissue Int. **42**(3), 145–156 (1988). https://doi.org/10.1007/BF02556327
33. Frost, H.M.: Perspectives: a proposed general model of the "mechanostat" (suggestions from a new skeletal-biologic paradigm). Anat. Rec. **244**(2), 139–147 (1996). https://doi.org/10.1002/(SICI)1097-0185(199602)244:2<139::AID-AR1>3.0.CO;2-X
34. Gao, J., Williams, J.L., Roan, E.: Multiscale modeling of growth plate cartilage mechanobiology. Biomech. Model. Mechanobiol (2016). https://doi.org/10.1007/s10237-016-0844-8
35. García-Aznar, J.M., Kuiper, J.H., Gómez-Benito, M.J., Doblaré, M., Richardson, J.B.: Computational simulation of fracture healing: influence of interfragmentary movement on the callus growth. J. Biomech. **40**(7), 1467–1476 (2007). https://doi.org/10.1016/j.jbiomech.2006.06.013
36. Garijo, N., Fernández, J.R., Pérez, M.A., García-aznar, J.M.: Numerical stability and convergence analysis of bone remodeling model. Comput. Methods Appl. Mech. Eng. **271**, 253–268 (2014). https://doi.org/10.1016/j.cma.2013.12.014
37. Giorgio, I., Andreaus, U., dell'Isola, F., Lekszycki, T.: Viscous second gradient porous materials for bones reconstructed with bio-resorbable grafts. Extreme Mech. Lett. **13**, 141–147 (2017). https://doi.org/10.1016/j.eml.2017.02.008
38. Giorgio, I., Andreaus, U., Lekszycki, T., Della Corte, A.: The influence of different geometries of matrix/scaffold on the remodeling process of a bone and bioresorbable material mixture with voids. Math. Mech. Solids **22**(5), 969–987 (2017)
39. Giorgio, I., Andreaus, U., Scerrato, D., Braidotti, P.: Modeling of a non-local stimulus for bone remodeling process under cyclic load: application to a dental implant using a bioresorbable porous material. Math. Mech. Solids **22**(9), 1790–1805 (2017)
40. Giorgio, I., Andreaus, U., Scerrato, D., dell'Isola, F.: A visco-poroelastic model of functional adaptation in bones reconstructed with bio-resorbable materials. Biomech. Model. Mechanobiol. **15**(5), 1325–1343 (2016). https://doi.org/10.1007/s10237-016-0765-6
41. Gomez-Benito, M.J., Garcia-Aznar, J.M., Kuiper, J.H., Doblaré, M.: Influence of fracture gap size on the pattern of long bone healing: a computational study. J. Theor. Biol. **235**(1), 105–119 (2005). https://doi.org/10.1016/j.jtbi.2004.12.023
42. Gundle, R., Joyner, C.J., Triffitt, J.T.: Human bone tissue formation in diffusion chamber culture in vivo by bone-derived cells and marrow stromal fibroblastic cells. Bone **16**(6), 597–601 (1995). https://doi.org/10.1016/8756-3282(95)00112-Q
43. Hansen, U., Zioupos, P., Simpson, R., Currey, J.D., Hynd, D.: The effect of strain rate on the mechanical properties of human cortical bone. J. Biomech. Eng. **130**(1), 11–18 (2008). https://doi.org/10.1115/1.2838032
44. Huiskes, R., Ruimerman, R., van Lenthe, G.H., Janssen, J.D.: Effects of mechanical forces on maintenance and adaptation of form in trabecular bone. Nature **405**(6787), 704–706 (2000). https://doi.org/10.1038/35015116
45. Huiskes, R., Van Driel, W.D., Prendergast, P.J., Søballe, K.: A biomechanical regulatory model for periprosthetic fibrous-tissue differentiation. J. Mater. Sci. Mater. Med. **8**(12), 785–788 (1997). https://doi.org/10.1023/A:1018520914512
46. Huiskes, R., Weinans, H., Grootenboer, H.J., Dalstra, M., Fudala, B., Slooff, T.J.: Adaptive bone-remodeling theory applied to prosthetic-design analysis. J. Biomech. **20**(11–12), 1135–1150 (1987). https://doi.org/10.1016/0021-9290(87)90030-3
47. Isaksson, H., van Donkelaar, C.C., Huiskes, R., Ito, K.: Corroboration of mechanoregulatory algorithms for tissue differentiation during fracture healing: comparison with in vivo results. Anticancer Res. **24**(5), 898–907 (2006). https://doi.org/10.1002/jor
48. Isaksson, H., Gröngröft, I., Wilson, W., Van Donkelaar, C.C., Ven Rietbergen, B., Tami, A., Ito, K.: Remodeling of fracture callus in mice is consistent with mechanical loading and bone remodeling theory. J. Orthop. Res. **27**(5), 664–672 (2009). https://doi.org/10.1002/jor.20725
49. Jones, L.C., Frondoza, C., Hungerford, D.S.: Immunohistochemical evaluation of interface membranes from failed cemented and uncemented acetabular components. J. Biomed. Mater. Res. **48**(6), 889–898 (1999). https://doi.org/10.1002/(SICI)1097-4636(1999)48:6<889::AID-JBM19>3.0.CO;2-S
50. Joos, U., Büchter, A., Wiesmann, H.-P., Meyer, U.: Strain driven fast osseointegration of implants. Head Face Med. **1**, 6 (2005). https://doi.org/10.1186/1746-160X-1-6
51. Kalfas, I.H.: Principles of bone healing. Neurosurg. Focus **10**(4), 1–4 (2001)
52. Klika, V., Angelés, M., García-Aznar, M.J., Maršík, F., Doblaré, M.: A coupled mechano-biochemical model for bone adaptation. Math. Biol. **69**, 1383–1429 (2014). https://doi.org/10.1007/s00285-013-0736-9
53. Komarova, S.V., Smith, R.J., Dixon, S.J., Sims, S.M., Wahl, L.M.: Mathematical model predicts a critical role for osteo-clast autocrine regulation in the control of bone remodeling. Bone **33**, 206–215 (2003). https://doi.org/10.1016/S8756-3282(03)00157-1
54. Kraaij, G., Zadpoor, A.A., Tuijthof, G.J.M., Dankelman, J., Nelissen, R.G.H.H., Valstar, E.R.: Mechanical properties of human bone-implant interface tissue in aseptically loose hip implants. J. Mech. Behav. Biomed. Mater. **38**, 59–68 (2014). https://doi.org/10.1016/j.jmbbm.2014.06.010
55. Kular, J., Tickner, J., Chim, S.M., Xu, J.: An overview of the regulation of bone remodelling at the cellular level. Clin. Biochem. **45**(12), 863–873 (2012). https://doi.org/10.1016/j.clinbiochem.2012.03.021
56. Kuzyk, P., Schemitsch, E.: The basic science of peri-implant bone healing. Indian J. Orthop. **45**(2), 108–115 (2011)
57. Lacroix, D., Prendergast, P.J.: A mechano-regulation model for tissue differentiation during fracture healing: analysis of gap size and loading. J. Biomech. **35**(9), 1163–1171 (2002). https://doi.org/10.1016/S0021-9290(02)00086-6
58. Lerebours, C., Buenzli, P.R., Scheiner, S., Pivonka, P.: A multiscale mechanobiological model of bone remodelling predicts site-specific bone loss in the femur during osteoporosis and mechanical disuse. Biomech. Model. Mechanobiol. **15**(1), 43–67 (2016). https://doi.org/10.1007/s10237-015-0705-x
59. Li, J., Li, H., Shi, L., Fok, A.S.L., Ucer, C., Devlin, H., Silikas, N.: A mathematical model for simulating the bone remodeling process under mechanical stimulus. Dent. Mater. **23**(9), 1073–1078 (2007). https://doi.org/10.1016/j.dental.2006.10.004
60. Lieberman, D.E., Polk, J.D., Demes, B.: Predicting long bone loading from cross-sectional geometry. Am. J. Phys. Anthropol. **123**(2), 156–171 (2004). https://doi.org/10.1002/ajpa.10316
61. Liu, X., Niebur, G.L.: Bone ingrowth into a porous coated implant predicted by a mechano-regulatory tissue differentiation algorithm. Biomech. Model. Mechanobiol. **7**(4), 335–344 (2008). https://doi.org/10.1007/s10237-007-0100-3

62. Mack, P., LaChance, P., Vose, G., Vogt, F.: Bone demineralization of foot and hand of Gemini-Titan IV, V and VII astronauts during orbital flight. Am. J. Roentgenol. Radium Ther. Nucl. Med. **100**(3), 503–511 (1967)

63. Malo, M.K.H., Rohrbach, D., Isaksson, H., Töyräs, J., Jurvelin, J.S., Tamminen, I.S., Raum, K.: Longitudinal elastic properties and porosity of cortical bone tissue vary with age in human proximal femur. Bone **53**(2), 451–458 (2013). https://doi.org/10.1016/j.bone.2013.01.015

64. Martin, T.J., Seeman, E.: Bone remodelling: its local regulation and the emergence of bone fragility. Best Pract. Res. Clin. Endocrinol. Metab. **22**(5), 701–722 (2008). https://doi.org/10.1016/j.beem.2008.07.006

65. Moerman, A., Zadpoor, A.A., Oostlander, A., Schoeman, M., Rahnamay Moshtagh, P., Pouran, B., Valstar, E.: Structural and mechanical characterisation of the peri-prosthetic tissue surrounding loosened hip prostheses. An explorative study. J. Mech. Behav. Biomed. Mater. **62**, 456–467 (2016). https://doi.org/10.1016/j.jmbbm.2016.04.009

66. Mukherjee, K., Gupta, S.: Simulation of tissue differentiation around acetabular cups?: the effects of implant-bone relative displacement and polar gap. Adv. Biomech. Appl. **1**(2), 95–109 (2014)

67. Nakagaki, S., Iijima, M., Handa, K., Koike, T., Yasuda, Y., Saito, T., Mizoguchi, I.: Micro-CT and histologic analyses of bone surrounding immediately loaded miniscrew implants: comparing compression and tension loading. Dent. Mater. J. **33**(2), 196–202 (2014). https://doi.org/10.4012/dmj.2013-223

68. Neale, S.D., Fujikawa, Y., Sabokbar, A., Gundle, R., Murray, D.W., Graves, S.E., Howie, D.W., Athanasou, N.A.: Human bone-derived cells support formation of human osteoclasts from arthroplasty-derived cells in vitro. J. Bone Jt. Surg. Br. Vol. **82**(6), 892–900 (2000). https://doi.org/10.1302/0301-620x.82b6.10175

69. Panteli, M., Pountos, I., Jones, E., Giannoudis, P.V.: Biological and molecular profile of fracture non-union tissue: current insights. J. Cell. Mol. Med. **19**(4), 685–713 (2015). https://doi.org/10.1111/jcmm.12532

70. Pivonka, P., Zimak, J., Smith, D.W., Gardiner, B.S., Dunstan, C.R., Sims, N.A., Mundy, G.R.: Model structure and control of bone remodeling?: a theoretical study. Bone **43**, 249–263 (2008). https://doi.org/10.1016/j.bone.2008.03.025

71. Prendergast, P.J., Huiskes, R., Søballe, K.: Biophysical stimuli on cells during tissue differentiation at implant interfaces. J. Biomech. **30**(6), 539–548 (1997). https://doi.org/10.1016/S0021-9290(96)00140-6

72. Quinn, J., Joyner, C., Triffitt, J.T., Athanasou, N.A.: Polymethylmethacrylate-induced inflammatory macrophages resorb bone. J. Bone Joint Surg. **74**(5), 652–658 (1992)

73. Reilly, G.C., Currey, J.D.: The development of microcracking and failure in bone depends on the loading mode to which it is adapted. J. Exp. Biol. **202**(5), 543–552 (1999)

74. Reilly, G.C., Currey, J.D.: The effects of damage and microcracking on the impact strength of bone **33**, 337–343 (2000)

75. Rho, J. Y., Kuhn-Spearing, L., & Zioupos, P. (1998). Mechanical properties and the hierarchical structure of bone. Med. Eng. Phys. **20**(2), 92–102. Retrieved from http://www.ncbi.nlm.nih.gov/pubmed/9679227

76. Rho, J. Y., Roy, M., & Pharr, G. M. (2000). Comments on "Elastic modulus and hardness of cortical and trabecular bone lamellae measured by nanoindentation in the human femur". J. Biomech. **33**(10), 1335–7. Retrieved from http://www.ncbi.nlm.nih.gov/pubmed/11023378

77. Rolfson, O., Kärrholm, J., Dahlberg, L.E., Garellick, G.: Patient-reported outcomes in the Swedish hip arthroplasty register: results of a nationwide prospective observational study. J. Bone Joint Surg. Br. Vol. **93**(7), 867–875 (2011). https://doi.org/10.1302/0301-620X.93B7.25737

78. Rubin, J., Rubin, C., Rae, C.: Molecular pathways mediating mechanical signaling in bone. Gene **367**, 1–16 (2006). https://doi.org/10.1016/j.gene.2005.10.028

79. Salisbury Palomares, K.T., Gleason, R.E., Mason, Z.D., Cullinane, D.M., Einhorn, T.A., Gerstenfeld, L.C., Morgan, E.F.: Mechanical stimulation alters tissue differentiation and molecular expression during bone healing. J. Orthop. Res. **27**(9), 1123–1132 (2009). https://doi.org/10.1002/jor.20863

80. Scala, I., Spingarn, C., Rémond, Y., Madeo, A., George, D.: Mechanically-driven bone remodeling simulation: application to LIPUS treated rat calvarial defects. Math. Mech. Solids. **22**(10), 1976–1988 (2016). https://doi.org/10.1177/1081286516651473

81. Schindeler, A., McDonald, M.M., Bokko, P., Little, D.G.: Bone remodeling during fracture repair: the cellular picture. Semin. Cell Dev. Biol. **19**(5), 459–466 (2008). https://doi.org/10.1016/j.semcdb.2008.07.004

82. Schmitt, M., Allena, R., Schouman, T., Frasca, S., Collombet, J.M., Holy, X., Rouch, P.: Diffusion model to describe osteogenesis within a porous titanium scaffold. Comput. Methods Biomech. Biomed. Eng. **16**(2015), 1–9 (2015). https://doi.org/10.1080/10255842.2014.998207

83. Søballe, K., Hansen, E.S., Brockstedt-Rasmussen, H., Bünger, C.: Hydroxyapatite coating converts fibrous tissue to bone around loaded implants. J. Bone Joint Surg. (Br.) **75**(2), 270–278 (1993)

84. Spingarn, C., Wagner, D., Rémond, Y., George, D.: Multiphysics of bone remodeling: a 2D mesoscale activation simulation. Bio-Med. Mater. Eng. **28**(1), S153–S158 (2017)

85. Srinivasan, S., Agans, S.C., King, K.A., Moy, N.Y., Poliachik, S.L., Gross, T.S.: Enabling bone formation in the aged skeleton via rest-inserted mechanical loading. Bone **33**(6), 946–955 (2003). https://doi.org/10.1016/j.bone.2003.07.009

86. Srinivasan, S., Gross, T.S.: Canalicular fluid flow induced by bending of a long bone. Med. Eng. Phys. **22**(2), 127–133 (2000). https://doi.org/10.1016/S1350-4533(00)00021-7

87. Srinivasan, S., Weimer, D.A., Agans, S.C., Bain, S.D., Gross, T.S.: Low-magnitude mechanical loading becomes osteogenic when rest is inserted between each load cycle. J. Bone Miner. Res. **17**(9), 1613–1620 (2002). https://doi.org/10.1359/jbmr.2002.17.9.1613

88. Stanford, C.M., Brand, R.A.: Toward an understanding of implant occlusion and strain adaptive bone modeling and remodeling. J. Prosthet. Dent. **81**(5), 553–561 (1999). https://doi.org/10.1016/S0278-2391(00)90358-6

89. Stokes, I.A.F., Clark, K.C., Farnum, C.E., Aronsson, D.D.: Alterations in the growth plate associated with growth modulation by sustained compression or distraction. Bone **41**(2), 197–205 (2007). https://doi.org/10.1016/j.bone.2007.04.180

90. Strehle, J., Del Notaro, C., Orler, R., Isler, B.: The outcome of revision hip arthroplasty in patients older than age 80 years. J. Arthroplasty **15**(6), 690–697 (2000). https://doi.org/10.1054/arth.2000.7111

91. Tiwari, A.K., Prasad, J.: Computer modelling of bone's adaptation: the role of normal strain, shear strain and fluid flow. Biomech. Model. Mechanobiol. **16**(2), 1–16 (2016). https://doi.org/10.1007/s10237-016-0824-z

92. Turner, C.H.: Three rules for bone adaptation to mechanical stimuli. Bone **23**(5), 399–407 (1998). https://doi.org/10.1016/S8756-3282(98)00118-5
93. Wang, H., Hao, Z., Wen, S.: Finite element analysis of the effect of medullary contact on fracture healing and remodeling in the intramedullary interlocking nail-fixed tibia fracture. Int. J. Numer. Methods Biomed. Eng. **33**(4), 1–13 (2017). https://doi.org/10.1002/cnm.2816
94. Wiscott, H., Belser, U.: Lack of integration of smooth titanium surfaces: a working hypothesis based on strains generated in the surrounding bone. Clin. Oral Implant Res. **10**, 429–444 (1999)
95. Zioupos, P., Currey, J.D.: The extent of microcracking and the morphology of microcracks in damaged bone. J. Mater. Sci. **29**(4), 978–986 (1994). https://doi.org/10.1007/BF00351420
96. Zioupos, P., Hansen, U., Currey, J.D.: Microcracking damage and the fracture process in relation to strain rate in human cortical bone tensile failure. J. Biomech. **41**(14), 2932–9 (2008). https://doi.org/10.1016/j.jbiomech.2008.07.025